Chapter-5

EQUILIBRIUM SOLAR PLASMA CHARACTERIZATION IN REFINED GES-MODEL FABRIC WITH NEGATIVE IONS

Abstract: *The GES-model, studying the SWP origin from the SIP via the SSB, is revaluated by the inclusion of the realistic negative ionic species for the first time. The plasma medium consists of the Boltzmann electrons along with the fluidic positive and negative ions. The model structuring equations for the bi-scaled plasma system are methodically constructed. A numerical analysis is carried out to study the key solar plasma features, such as the plasma constituent population distribution, Mach number, electric potential, electric current, etc. Lastly, a comparative evaluation of our findings with the previously reported results is performed for testing its validation illustratively*[†].

5.1 INTRODUCTION

The entire solar plasma system consisting of the bounded Sun and its unbounded surrounding atmosphere has been a mysterious natural plasma laboratory for decades, yet to be well understood. The most challenging aspect of such solar systems lies basically in understanding the complex nature of the solar wind flow dynamics and associated structure formation. It is extensively found in the literature that the investigation of the normal stellar systems, like the Sun and its atmosphere, has been performed on various plausible theoretical model formalisms. However, it may be noteworthy that, one of the unaddressed major aspects in this important direction of solar exploration lies in the fact that the presence of diverse negative ions in the solar plasma dynamics has always been ignored in solar plasma theorization in the past as far as seen in available literature [1, 2].

The role of negative ions is well known to be unavoidable in the electromagnetic structurization of such stellar systems. It is found, in the literature [3], that this has been one of the significant problems in stellar astrophysics in the early decades of the 20th century to explain radiation absorption in the exterior regions of cool stellar environs, such as the Sun and its atmosphere. It has been believed that the sustained opacity in the

[†]Sarma, P. and Karmakar, P. K. Effects of negative ions on equilibrium solar plasmas in the fabric of gravito-electrostatic sheath model. *Scientific Reports*, Under Review, 2023.

visible frequencies of the electromagnetic spectrum is caused due to the presence of the metal atoms with an abundance ratio 1:50 with respect to hydrogen. However, in 1939, R. Wildt has reported that the H^- ion dominates the visible opacity in the sun-like stars with photospheric temperature less than 7000 K, with the metal:hydrogen abundance ratio 1:1000 [3, 4]. It is now evident that, in the cool stellar plasma systems, the photoionization of the metal atoms provides the electrons that produce the H^- ion [3]. With advancement in the spectrophotometric analytical techniques, it is now well established that except H^-, several other atomic as well as molecular negative ions, like Cl^-, C^-, S^-, OH^-, C_2^-, CN^-, SH^- and H_2O^- have significant contributions towards the continuous opacity of the late type stellar spectra [5, 6]. Nevertheless, the role of realistic negative ions, as highlighted previously, in the stellar plasma evolution, has never been explored. In fact, any investigation of the solar plasma dynamics and equilibrium features in the realistic circumstances without considering the role of negative ionic species is both improper and inadequate. Accordingly, such studies pose another venture in exploring the solar plasma model characteristics moderated in the presence of diverse negative ionic species evolving in the real solar plasma system.

As a consequence of the above motivating factual scenarios, the presented investigation characterizes the role of the negative ions in the solar plasma evolution on the original gravito-electrostatic sheath (GES)-fabric founded on the basic plasma-wall interaction physics [7]. It illustratively portrays the relevancy of negative ions in the equilibrium solar plasma processes and subsequent equilibrium structurization in the bi-scaled solar plasma system, i.e., solar interior plasma (SIP) and solar wind plasma (SWP) coupled via the interfacial solar surface boundary (SSB). Additionally, a comparative reliability assessment is performed in light of the key observed solar properties drawn from various observational missions, such as the Parker Solar Probe (PSP), Helios, Wind, Cluster, and so forth [5, 6, 8-10]. On realistic applications, the proposed analytical study could be extensively useful in understanding the role of the naturalistic negative ions in the equilibrium structure analysis of the Sun and other normal sun-like stars with intermediate surface temperatures in a broader stellar astrophysical perspective.

5.2 SOLAR PLASMA MODEL FORMULATION

We consider the entire solar plasma system as a complex fluid medium composed of three constitutive species, such as electrons, positive ions (protons), and negative ions (heterogeneous). The non-gravitating lighter (inertialess) electrons are described by the

Maxwell-Boltzmann thermo-statistical distribution law. The gravitating heavier (inertial) positive (negative) ions are treated in the fluidic framework. The entire solar plasma model is assumed to be in a spherically symmetric geometry. It enables us to simplify the 3D solar problem as a reduced 1D one. It deals with the radial dependency of the relevant physical parameters only, because the polar and azimuthal counterparts are relaxed fully without any loss of generality [11, 12]. The plasma species form an isothermal hydrostatic equilibrium configuration throughout the entire bounded solar plasma system with the presumed global quasi-neutrality. This quasi-neutrality is well justifiable here on the grounds of asymptotically zero-value of the Debye-to-Jeans length scale ratio as already found in diverse realistic astronomical circumstances [7].

It is clearly perceptible from the gravito-thermal coupling constants of the plasma species [7, 13] that the inertialess electrons are capable of nimbly flying away from the considered plasma volume against the self-gravitational potential barrier at the cost of their thermal (kinetic) energy alone unlike the inertial ions. In a broader sense, the constitutive positive and negative ions cannot overcome the self-gravitational barrier hindrance with their thermal energy alone. This is the key phenomenon responsible for the consequent space-charge polarization effects, leading thereby to the formation of the GES structure. It is noteworthy here that, the basic physical insights of the original GES-model are well founded on the same plasma-wall interaction processes, as reported previously in analogy with the laboratory confined plasmas [7, 13]. Thus, with all these factual reservations in our model formulation, we propose a continued exploration on the equilibrium solar plasma characteristic features in the presence of diverse negative ionic species in real astronomical circumstances for the first time.

5.2.1 SIP FORMALISM

The considered SIP system consists of inertialess electrons (Boltzmann), inertial positive ions (fluid), and inertial negative ions (fluid) coupled via the electro-gravitational Poisson equations representing potential evolutions at the cost of density fields. The electronic dynamics is accordingly governed by the Maxwell-Boltzmann thermo-statistical distribution law expressed in all the generic notations [7] as

$$n_e = n_{e0}\exp\left(\frac{e\varphi}{k_B T_e}\right). \tag{5.1}$$

The dynamics of the constitutive positive ions is governed by the continuity equation (flux conservation), momentum equation (linear momentum conservation), and isothermal equation of state, given respectively in the generic notations [14] as

$$\partial_t n_+ + v_+(\partial_r n_+) + n_+(\partial_r v_+) + \frac{2}{r}(n_+ v_+) = 0, \tag{5.2}$$

$$m_+ n_+ [\partial_t v_+ + v_+(\partial_r v_+)] = -e n_+(\partial_r \varphi) - \partial_r P_T - m_+ n_+(\partial_r \psi), \tag{5.3}$$

$$P_{T+} = n_+ k_B T_+ . \tag{5.4}$$

The negative ion dynamics follows the similar equations cast respectively as

$$\partial_t n_- + v_-(\partial_r n_-) + n_-(\partial_r v_-) + \frac{2}{r}(n_- v_-) = 0, \tag{5.5}$$

$$m_- n_- [\partial_t v_- + v_-(\partial_r v_-)] = e n_-(\partial_r \varphi) - \partial_r P_T - m_- n_-(\partial_r \psi), \tag{5.6}$$

$$P_{T-} = n_- k_B T_- . \tag{5.7}$$

The model closure is finally obtained with the help of the electro-gravitational Poisson equations for the corresponding potential distributions given respectively in usual notations as

$$\partial_r^2 \varphi + \frac{2}{r}(\partial_r \varphi) = \frac{e}{\varepsilon_0}(n_e + n_- - n_+), \tag{5.8}$$

$$\partial_r^2 \psi + \frac{2}{r}(\partial_r \psi) = 4\pi G(m_+ n_+ + m_- n_-). \tag{5.9}$$

Finally, the electric current density associated with the SIP is cast in usual symbols as

$$j_{SIP} = n_+ e\left[-\sqrt{2r(\partial_r \psi)} - \sqrt{\left(\frac{2e}{m_+}\right) r(\partial_r \varphi)}\right] + n_- e\left[-\sqrt{2r(\partial_r \psi)} + \sqrt{\left(\frac{2e}{m_-}\right) r(\partial_r \varphi)}\right] + n_e e\sqrt{\left(\frac{2e}{m_e}\right) r(\partial_r \varphi)}. \tag{5.10}$$

All the customary notations with their physical significances in the above un-normalized equations are detailed in Table 5.1.

Table 5.1: Symbol and significance

Symbol	Mathematical significance	Physical significance
r	Radial distance (heliocentric)	Distance of an observation point from the reference heliocenter in spherical polar coordinates
t	Time coordinate	Time between two events as measured by an observer static with respect to heliocenter
n_e	Electron number density	Number of electron per unit volume in the

		plasma system
n_{e0}	Equilibrium electron number density	Equilibrium number of electron per unit quasi-neutral plasma volume
T_e	Electron temperature	Electronic thermal (kinetic) potential causing directive heat flow
m_e	Electron mass	Measure of electronic resistance to change of its state due to a force field (m_e = 9.10 × 10^{-31} kg)
e	Electronic (protonic) charge unit	Property of an electron (proton) that causes it to experience a force when placed in an electromagnetic field (1.60 × 10^{-19} C)
$n_{+(-)}$	Positive (negative) ion number density	Number of positive (negative) ions per unit plasma volume
$n_{+(-)0}$	Equilibrium positive (negative) ion number density	Equilibrium number of positive (negative) ions per unit quasi-neutral plasma volume
n_0	Equilibrium (mean) solar plasma density	Equilibrium particle number per unit quasi-neutral solar plasma volume
$T_{+(-)}$	Positive (negative) ion temperature	Ionic (positive/negative) thermal (kinetic) potential causing bulk plasma heat flow
$m_{+(-)}$	Positive (negative) ion mass	Resistive measure of positive (negative) ions against a net force field causing its change of state ($m_{+(-)} \sim 1.67 \times 10^{-27}$ kg)
$v_{+(-)}$	Positive (negative) ion velocity	Directional speed of positive (negative) ion seen by a static observer with respect to the heliocenter
$u_{+(-)}$	Bohm velocity	Directional speed of positive (negative) ion to the plasma sheath for compensating their loss from the sheath towards a floating condition
φ	Electric potential	Amount of work done to move a unit charge from a reference point (φ=0) to a specific point against the electric field.

ψ	Gravitational potential	Amount of work done to move a unit mass from a reference point (ψ=0) to a specific point against the gravitational field.
$P_{T+(-)}$	Positive (negative) ion partial pressure	Normal force per unit area applied by only a positive (negative) ionic fluid element to an object over which that force is distributed.
P_T	Total pressure	Total normal force per unit area applied by a plasma fluid element to an object over which that force is distributed.
$j_{SIP\ (SWP)}$	SIP (SWP) electric current density	Amount of charge that flows through a unit area of SIP (SWP) elemental cross-section per unit time.
k_B	Boltzmann constant	It is a universal coupling constant between temperature and kinetic energy. (k_B=1.38×10^{-23} J K^{-1})
ε_0	Vacuum permittivity	A measure of the ability of electrical fields to pass through vacuum (ε_0=8.85 × 10^{-12} C^2 N^{-1} m^{-2})
λ_{De}	Solar electron Debye length	A physical scale characterizing the minimum electrostatic polarization length (λ_{De}=2×10^{-12} m)
λ_J	Jeans scale length	Critical scale size representing a stable self-gravitating cloud (in hydrostatic equilibrium, λ_J ~ 10^8 m)
G	Universal gravitational constant	A coupling constant signifying Newton's gravitational force field between two gravitating bodies (G=6.67×10^{-11} N m^2 kg^{-2})

Now, in order to explore the equilibrium solar structure numerically according to our model formalism, equations (5.1)-(5.10) are first expressed in the time-stationary normalized form following a standard astronomical normalization scheme [7], as detailed in Table 5.2. Accordingly equations (5.1)-(5.10) can respectively be written in the normalized forms cast as

$$N_e = \exp(\Phi), \tag{5.11}$$

$$\frac{1}{N_+}\left(\partial_\xi N_+\right)+\frac{1}{M_+}\left(\partial_\xi M_+\right)+\frac{2}{\xi}=0, \tag{5.12}$$

$$M_+\left(\partial_\xi M_+\right)=-\partial_\xi \Phi-\left(\frac{T_+}{T_e}\right)\frac{1}{N_+}\left(\partial_\xi N_+\right)-\partial_\xi \Psi, \tag{5.13}$$

$$P^*_{T+}=\left(\frac{n_{+0}k_B T_+}{P_0}\right)N_+, \tag{5.14}$$

$$\frac{1}{N_-}\left(\partial_\xi N_-\right)+\frac{1}{M_-}\left(\partial_\xi M_-\right)+\frac{2}{\xi}=0, \tag{5.15}$$

$$M_-\left(\partial_\xi M_-\right)=\frac{m_+}{m_-}\left(\partial_\xi \Phi\right)-\frac{m_+}{m_-}\left(\frac{T_-}{T_e}\right)\frac{1}{N_-}\left(\partial_\xi N_-\right)-\partial_\xi \Psi, \tag{5.16}$$

$$P^*_{T-}=\left(\frac{n_{-0}k_B T_-}{P_0}\right)N_-, \tag{5.17}$$

$$\partial^2_\xi \Phi+\frac{2}{\xi}\left(\partial_\xi \Phi\right)=\left(\frac{\lambda_J}{\lambda_{De}}\right)^2\left[(1-\delta)N_e+\delta N_- - N_+\right], \tag{5.18}$$

$$\partial^2_\xi \Psi+\frac{2}{\xi}\left(\partial_\xi \Psi\right)=\left[N_+ +\delta N_-\right], \tag{5.19}$$

$$J_{SIP}=N_+\left[-\sqrt{2\xi(\partial_\xi \Psi)}-\sqrt{2\xi(\partial_\xi \Phi)}\right]+\delta N_-\left[-\sqrt{2\xi\left(\partial_\xi \Psi\right)}+\sqrt{2\xi\left(\frac{m_+}{m_-}\right)\left(\partial_\xi \Phi\right)}\right]+(1-\delta)N_e\sqrt{2\xi\left(\frac{m_+}{m_e}\right)\left(\partial_\xi \Phi\right)}. \tag{5.20}$$

It is worth mentioning that time-stationary coupled equations (5.11)-(5.20) govern the steady-state dynamics of the self-gravitating SIP and the subsequent equilibrium structure of the GES in a closed form modified due to the presence of considered negative ions. The normalized equations above are now coupled to obtain a closed set of time-stationary first-order differential equations for the description of the equilibrium SIP evolution. It is now seen from the above that the resulting SIP system is sensitive to the relevant parametric variations, such as the equilibrium negative-to-positive ion density ratio (δ), positive-to-negative ion mass ratio (m_i/m_-), positive ion-to-electron temperature ratio (T_i/T_e), and negative ion-to-electron temperature ratio (T_-/T_e). It is to be noted, specifically in the mathematical perspective that the δ-sensitivity arises from equations (5.18)-(5.20). The m_i/m_--sensitivity originates from equation (5.16) and equation (5.20). The T_i/T_e- and T_-/T_e-sensitivities appear from equation (5.13) and equation (5.16), respectively. The fourth-order Runge-Kutta (RK-IV) method is applied for the steady-state SIP analysis with the sensible initial and input values, as depicted in

Table 5.3, using MATLAB [7, 15]. In the subsequent analysis, we replace the positive ionic symbol "+", as in the equations, with "i", as per the usual convention.

Table 5.2: Astronomical normalization scheme

Normalized symbol	Normalizing parameter	Typical value [14]
$\xi = r/\lambda_J$	Jeans scale (λ_J)	2×10^8 m
$N_e = n_e/n_{e0}$	Equilibrium quasi-neutral electron number density (n_{e0}=n_0-n_{-0})	Conditional (~10^{30} m^{-3})
$N_{+(-)} = n_{+(-)}/n_{+(-)0}$	Equilibrium quasi-neutral positive (negative) ion number density ($n_{+(-)0}$, where, n_{+0}=n_0=n_{e0}+n_{-0})	n_0=10^{30} m^{-3}
$M_{+(-)} = v_{+(-)}/c_s$	SIP sound speed (c_s= $\sqrt{k_B T_e/m_+}$)	3×10^5 m s^{-1}
$\Phi = e\varphi/k_B T_e$	SIP electron thermal potential $(k_B T_e/e)$	10^3 V
$\Psi = \psi/c_s^2$	Square of the SIP sound speed (c_s^2, kinetic acoustic potential)	9×10^{10} m^2 s^{-2}
$P^*_{T+(-)} = P_{T+(-)}/P_0$	Mean SIP pressure (P_0)	10^{14} N m^{-2}
$J_{SIP(SWP)} = j_{SIP(SWP)}/j_B$	SIP Bohm electric current density (j_B)	4.8×10^{16} A m^{-2}

Table 5.3: Initial and input value

S. No.	Physical parameter	SIP input	SWP input
1	Radial distance	10^{-3}	3.75
2	Gravitational field strength	10^{-5}	NA
3	Electric potential	10^{-4}	-1.172
4	Electric field strength	10^{-4}	-0.65
5	Positive ion number density	10^{-4}	Conditional
6	Positive ion Mach number	10^{-4}	Conditional

7	Negative ion number density	10^{-4}	Conditional
8	Negative ion Mach number	10^{-4}	Conditional

5.2.2 SWP FORMALISM

It is already known that, as the bounded SIP transforms into the unbounded SWP, the Newtonian gravity changes from the self-gravity (extended source) to an external gravity (point source of mass M_Θ) without any loss in the macroscopic description of the integrated original solar plasma system [7]. Accordingly, the SWP-fluid dynamics is dictated by a similar set of governing equations as in the SIP case, except the plasma self-gravity (internal) now gets replaced with the inverse-square point-like Newtonian gravity (external). It hereby makes the self-gravitational Poisson equation redundant [7].

The SWP constitutive electrons follow the same Maxwell-Boltzmann thermo-statistical distribution law as in the SIP description, expressed as

$$n_e = n_{e0}\exp\left(\frac{e\varphi}{k_B T_e}\right). \tag{5.21}$$

The continuity equation, momentum equation and the equation of state followed by the positive ions are given respectively in a similar manner as

$$\partial_t n_+ + v_+\left(\partial_r n_+\right) + n_+\left(\partial_r v_+\right) + \frac{2}{r}\left(n_+ v_+\right) = 0, \tag{5.22}$$

$$m_+ n_+\left[\partial_t v_+ + v_+\left(\partial_r v_+\right)\right] = -e n_+\left(\partial_r \varphi\right) - \partial_r P_T - m_+ n_+\left(\frac{GM_\Theta}{r^2}\right), \tag{5.23}$$

$$P_{T+} = n_+ k_B T_+ . \tag{5.24}$$

Similarly, the equations dictating the dynamics of the negative ions in the SWP are cast respectively as

$$\partial_t n_- + v_-\left(\partial_r n_-\right) + n_-\left(\partial_r v_-\right) + \frac{2}{r}\left(n_- v_-\right) = 0, \tag{5.25}$$

$$m_- n_-\left[\partial_t v_- + v_-\left(\partial_r v_-\right)\right] = e n_-\left(\partial_r \varphi\right) - \partial_r P_T - m_- n_-\left(\frac{GM_\Theta}{r^2}\right), \tag{5.26}$$

$$P_{T-} = n_- k_B T_- . \tag{5.27}$$

The diverse constitutive species are coupled together with the help of the electrostatic Poisson equation and the net electric current density evolution equation, and are written respectively in the customary symbols as

$$\partial_r^2\varphi+\frac{2}{r}\left(\partial_r\varphi\right)=\frac{e}{\varepsilon_0}\left(n_e+n_--n_+\right), \tag{5.28}$$

$$j_{SWP}=n_+e\left[-\sqrt{2r\left(\frac{GM_\Theta}{r^2}\right)}-\sqrt{\left(\frac{2e}{m_+}\right)r\left(\partial_r\varphi\right)}\right]+n_-e\left[-\sqrt{2r\left(\frac{GM_\Theta}{r^2}\right)}+\sqrt{\left(\frac{2e}{m_-}\right)r\left(\partial_r\varphi\right)}\right]+n_ee\sqrt{\left(\frac{2e}{m_e}\right)r\left(\partial_r\varphi\right)}. \tag{5.29}$$

In order for a scale-invariant steady-state SWP description, equations (5.21)-(5.29) are transformed into the corresponding time-stationary normalized form, following the same astronomical normalization scheme as employed for the SIP. The normalized equations are respectively presented as

$$N_e=\exp\left(\Phi\right), \tag{5.30}$$

$$\frac{1}{N_+}\left(\partial_\xi N_+\right)+\frac{1}{M_+}\left(\partial_\xi M_+\right)+\frac{2}{\xi}=0, \tag{5.31}$$

$$M_+\left(\partial_\xi M_+\right)=-\partial_\xi\Phi-\left(\frac{T_+}{T_e}\right)\frac{1}{N_+}\left(\partial_\xi N_+\right)-\left(\frac{1}{c_s^2\lambda_J}\right)\frac{GM_\Theta}{\xi^2}, \tag{5.32}$$

$$P_{T+}^*=\left(\frac{n_{+0}k_BT_+}{P_0}\right)N_+, \tag{5.33}$$

$$\frac{1}{N_-}\left(\partial_\xi N_-\right)+\frac{1}{M_-}\left(\partial_\xi M_-\right)+\frac{2}{\xi}=0, \tag{5.34}$$

$$M_-\left(\partial_\xi M_-\right)=\frac{m_+}{m_-}\left(\partial_\xi\Phi\right)-\frac{m_+}{m_-}\left(\frac{T_-}{T_e}\right)\frac{1}{N_-}\left(\partial_\xi N_-\right)-\left(\frac{1}{c_s^2\lambda_J}\right)\frac{GM_\Theta}{\xi^2}, \tag{5.35}$$

$$P_{T-}^*=\left(\frac{n_{-0}k_BT_-}{P_0}\right)N_-, \tag{5.36}$$

$$\partial_\xi^2\Phi+\frac{2}{\xi}\left(\partial_\xi\Phi\right)=\left(\frac{\lambda_J}{\lambda_{De}}\right)^2\left[(1-\delta)N_e+\delta N_--N_+\right], \tag{5.37}$$

$$J_{SWP}=N_+\left[-\sqrt{\frac{2}{c_s^2\lambda_J}\left(\frac{GM_\Theta}{\xi}\right)}-\sqrt{2\xi\left(\partial_\xi\Phi\right)}\right]+\delta N_-\left[-\sqrt{\frac{2}{c_s^2\lambda_J}\left(\frac{GM_\Theta}{\xi}\right)}+\sqrt{2\xi\left(\frac{m_+}{m_-}\right)\left(\partial_\xi\Phi\right)}\right]+(1-\delta)N_e\sqrt{2\xi\left(\frac{m_+}{m_e}\right)\left(\partial_\xi\Phi\right)}. \tag{5.38}$$

It is noteworthy that time-stationary equations (5.30)-(5.38) dictate the steady-state nature of the non-gravitating SWP and its subsequent equilibrium flow dynamics relative to the SSB as its base in a closed analytic form, modified in the presence of considered negative ionic species. The resulting SWP system, as clearly evident from the coupled governing equations (equations (5.30)-(5.38)), is sensitive to the relevant parametric variations, such as δ, m_i/m_-, T_i/T_e, and T_-/T_e (as in the SIP). It is to be noted that the δ-sensitivity of the SWP system arises from equations (5.37)-(5.38). The m_i/m_--sensitivity originates from equation (5.35) and equation (5.38). The T_i/T_e- and T_-/T_e-

sensitivities in the SWP appear from equation (5.32) and equation (5.35), respectively. Accordingly, applying the SIP-specified initial and input values [7], as given in Table 5.3, the same RK-IV method, as in the SIP, is used herein for the SWP description numerically in a similar MATLAB computational platform [15].

5.3 RESULTS AND DISCUSSIONS

With the aim of portraying the complete steady-state structure of the solar plasma system based on our proposed GES-based model formalism modified with diverse negative ions, at first, the location of the new SSB formation by an exact gravito-electrostatic force-balancing is investigated and characterized. Accordingly, the strength of the self-gravity and electric field is plotted with the Jeans-normalized heliocentric radial distance for different equilibrium parametric variations, such as δ, m_i/m_-, T_i/T_e, and T_-/T_e as illustrated in figure 5.1. Here, the spatial grid size used is 0.25. It is found that the modified SSB divides the entire solar plasma volume into a bi-scaled system, bounded (SIP) and unbounded (SWP), separated by the interfacial SSB. This plasma system evolves alongside new changes parametrically introduced by the diverse negative ions included herewith for the first time.

It is interestingly observed that as the δ-value increases, the SSB and hence the SIP volume shrinks with a reduced maximum self-gravity magnitude of the bounded plasma mass. It can be well explained by the shielding nature of the plasma constituents by the opposite polarity species in the solar plasma medium. As δ increases, the negative ion density increases in accordance with the average solar plasma quasi-neutrality condition. The negative ions start to take part in the shielding mechanism of the positive ions together with the electrons. The electrons being negligible in size compared to the protons (positive ions), can shield the protons to a great extent. This overall high micro-scale neutrality facilitates self-gravitational condensation, resulting in high self-gravity at the SSB location. This inter-particle shielding between the negative and positive ions (protons) is not as compact as the shielding between the electrons and the positive ions. As a result, the self-gravitational condensation, as δ increases, is not as effective as in the lower δ-cases due to the presence of effective electrostatic interactions, resulting in low self-gravity in a reduced radial SSB location in a shrunk SIP volume.

It is noticed that the δ-sensitivity of the shrinking nature of the SIP volume, i.e., inward drifting nature of the SSB is high for high δ-values. The difference in the inward SSB-drifting nature becomes more prominent towards the high-δ region than that in the

low-δ region. This behaviour indicates that the SSB-location saturates itself to its radial magnitude in the solar plasma system with δ=0, as the negative ion concentration is gradually decreased. This means that the influence of the presence of negative ion becomes insignificant as their concentration is gradually lessened.

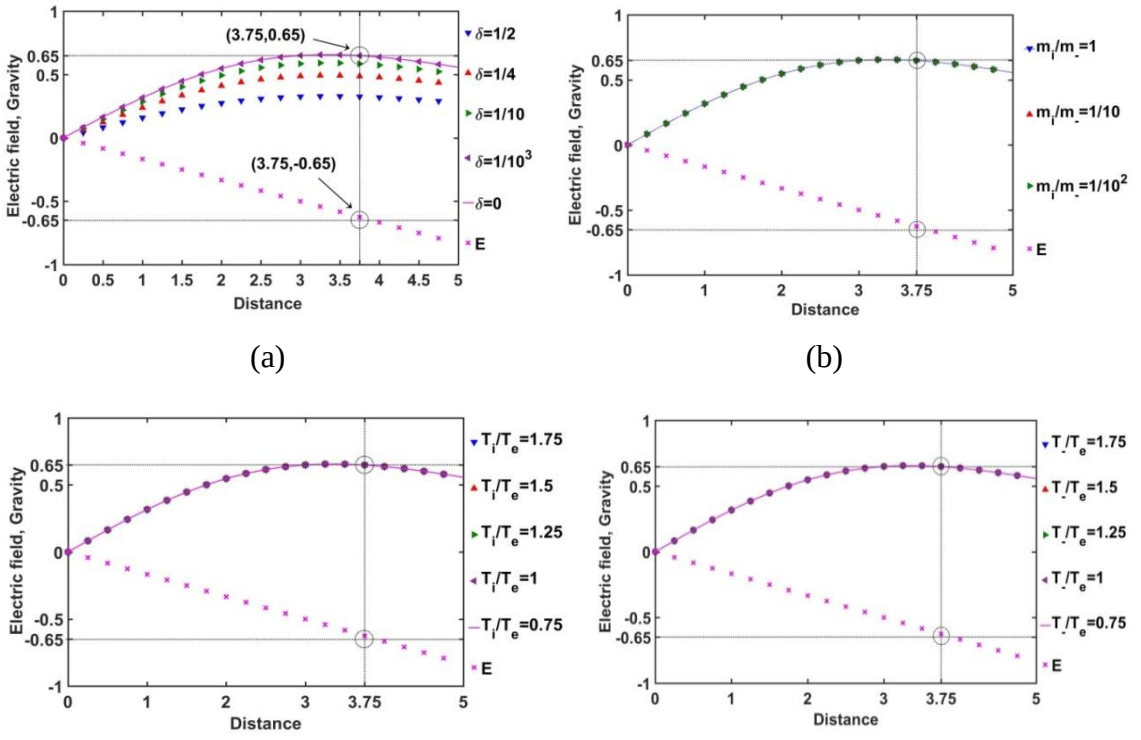

Figure 5.1: *Variation of the normalized electric field (E) and self-gravitational field (gravity) strength with the Jeans-normalized heliocentric radial distance for different values of the (a) equilibrium negative-to-positive ion density ratio (δ) with fixed m_i/m_-=1, T_i/T_e=1 and T_-/T_e=1; (b) positive-to-negative ion mass ratio (m_i/m_-) with fixed δ=1/1000, T_i/T_e=1 and T_-/T_e=1; (c) positive ion-to-electron temperature ratio (T_i/T_e) with fixed δ=1/1000, m_i/m_-=1 and T_-/T_e=1; and (d) negative ion-to-electron temperature ratio (T_-/T_e) with fixed δ=1/1000, m_i/m_-=1 and T_i/T_e=1.*

It is interestingly seen that for the δ=0 case, the SSB is not forming in our case at the 3.5 on the Jeans length scale, as reported previously in the original GES-model picture without negative ions [7, 14]. This shows the sensitiveness of our model to the inclusion of the negative ions. Though we impose the δ=0 condition based on average solar plasma behaviours, the negative ions are still available in the solar plasma system, as being seen pictorially in figure 5.10. So, it can be inferred that the presence of the

negative ions is responsible for the SSB location shifting to a new radial location ξ=3.75, against the pure GES SSB location at ξ=3.5 on the Jeans length scale [7], due to the shielding behavioural physics described above. It is found that the SSB-drifting nature is independent of the m_i/m_-, T_i/T_e, and T_-/T_e, as clearly depicted in figure 5.1.

After a methodological identification and characterization of the SSB, separating the SIP and SWP as the entire bi-scaled plasma system as above (figure 5.1), the investigated key results are described systematically in the following two subsections.

5.3.1 SIP-illustration

The SIP behaviours are analysed by studying the various properties of the bounded solar plasma mass, obtained from the numerical analysis of the combined model equations (equations (5.11)-(5.20)), with the initial inputs as presented in Table 5.3.

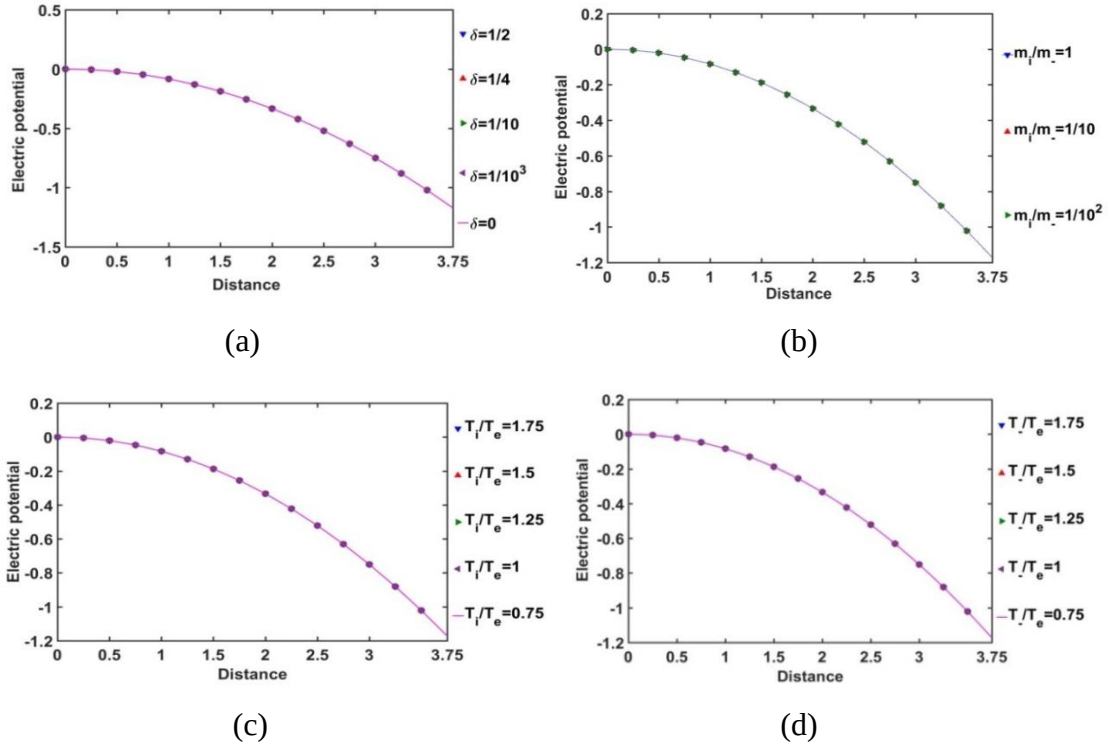

Figure 5.2: *Variation of the normalized SIP electric potential with the Jeans-normalized heliocentric radial distance for different values of (a) equilibrium negative-to-positive ion density ratio (δ) with fixed m_i/m_-=1, T_i/T_e=1 and T_-/T_e=1; (b) positive-to-negative ion mass ratio (m_i/m_-) with fixed δ=1/1000, T_i/T_e=1 and T_-/T_e=1; (c) positive ion-to-electron temperature ratio (T_i/T_e) with fixed δ=1/1000, m_i/m_-=1 and T_-/T_e=1; and (d) negative ion-to-electron temperature ratio (T_-/T_e) with fixed δ=1/1000, m_i/m_-=1 and T_i/T_e=1. The*

inner distinctions of these similar profiles obviously lie in the multi-parametric variations of current solar plasma relevance as shown herein.

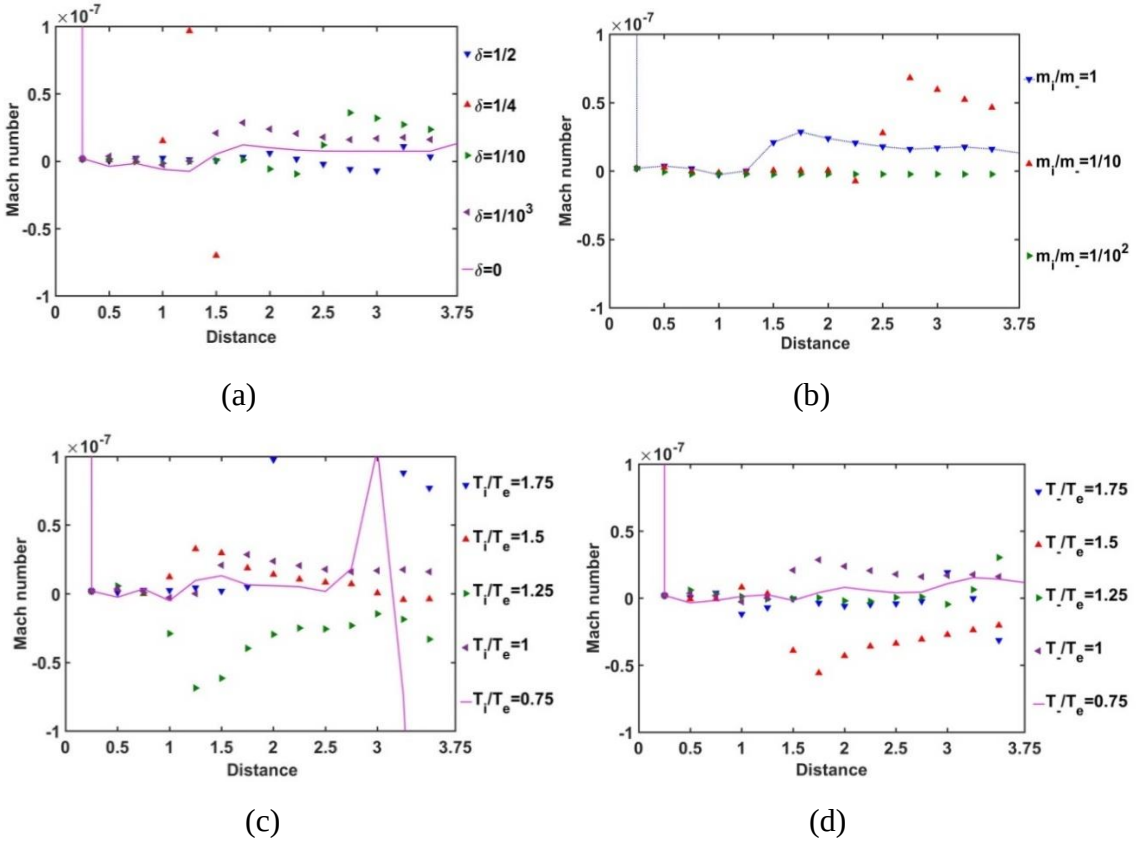

Figure 5.3: *Variation of the SIP Mach number with the Jeans-normalized heliocentric radial distance for different values of the (a) equilibrium negative-to-positive ion density ratio (δ) with fixed $m_i/m_-=1$, $T_i/T_e=1$ and $T_-/T_e=1$; (b) positive-to-negative ion mass ratio (m_i/m_-) with fixed $\delta=1/1000$, $T_i/T_e=1$ and $T_-/T_e=1$; (c) positive ion-to-electron temperature ratio (T_i/T_e) with fixed $\delta=1/1000$, $m_i/m_-=1$ and $T_-/T_e=1$; and (d) negative ion-to-electron temperature ratio (T_-/T_e) with fixed $\delta=1/1000$, $m_i/m_-=1$ and $T_i/T_e=1$.*

As depicted in figure 5.2, the profile of the normalized electric potential variation with the Jeans-normalized heliocentric radial distance is obtained for different values of δ, m_i/m_-, T_i/T_e and T_-/T_e. It is seen here that the electric potential is independent of the equilibrium negative ion population, mass of the negative ion as compared to the proton mass, and temperature of the positive and negative ions as compared to the electron temperature. The electric potential becomes negligible as the heliocenter is approached. It indicates high material density in the heliocentric region, which causes a significant shielding between the constitutive particles with opposite polarities. Away from the

heliocenter outwards, the material density decreases and particle diffusivity increases. As a consequence, the electrostatic polarization effects become more prominent, and so forth. The obtained results on the patterns of the spatial variation of electric potential are, in fact, found to be in a fair agreement with the recently reported thermo-statistically modified realistic GES-model description [14], thereby validating the reliability of our current analysis in the presence of diverse negative ionic species.

As depicted in figure 5.3, the spatial profile of the SIP Mach number is obtained for different indicated values of δ, m_i/m_-, T_i/T_e and T_-/T_e. It is noticed that the Mach number is very small in the SIP region. It is due to the very high plasma density in the SIP under self-gravitational action. The unidirectional ionic flow is significantly reduced by the inter-species collisions as well as the gravito-electrostatic interactions. The significant fluctuations in the Mach number with various parameters in the SIP are dependent on the radial material density fluctuations of the surrounding SIP medium. So, we can infer from here that the regions with a relatively high Mach number value have a drop in the material density as compared to the rest of the SIP-regions. As a result, for δ=1/4, there lies a rarefied region at ξ=1-1.5 (figure 5.3(a)); for m_i/m_-=1/10, a comparatively rarer region appears at ξ=2.5-3.75 (figure 5.3(b)); for T_i/T_e=0.75, a rarer region forms at ξ=3-3.75 (figure 5.3(c)), and for T_-/T_e=1.5, such a low-density region structurizes at ξ=1.5-2 (figure 5.3(d)), and so forth. It is found throughout that the SIP Mach number at the SSB comes out to be $M_{SSB}=1.3\times10^{-8}$ (figure 5.3).

In figure 5.4, the Bohm-normalized SIP electric current density variation with the Jeans-normalized heliocentric radial distance is numerically portrayed. It is seen that the current density decreases with an increase in δ, and vice-versa (figure 5.4(a)). It is consequent upon the fact that, as δ increases, the negative ion density increases, and vice-versa. So, we can infer that the presence of constitutive negative ions affects the net directional electric charge movement in the SIP medium significantly. It is also seen that the difference in the δ-sensitivities of the net electric current density decreases with an increase in δ. So, it can be inferred herewith that the current density saturates itself towards the SIP with the maximum δ-value as and when the δ-value increases. The relative mass of the positive ions with respect to the negative ions does not affect the net current density in the SIP (figure 5.4(b)). The SIP current density is sensitive to the relative temperature of the positive ion with respect to the electron temperature. As the ionic temperature increases, the current density decreases, and vice-versa. It implicates that the high thermo-mechanical energy of the protons affects the net charge directional

flow; the relatively cold positive ions result in a relatively high electric current. The difference in T_i/T_e-sensitivities of the net SIP current density decreases with an increase in the T_i/T_e-value (figure 5.4(c)). So, the net electric current density saturates itself to its saturation value in the plasma medium of high ionic temperature with respect to the electronic temperature as the T_i/T_e-value increases. However, interestingly, the temperature and hence, the kinetic energy of the considered negative ions does not influence the net charge directional flow contributed by the background existing positive ions on the SIP scale (figure 5.4(d)). It enables us to infer here that, due to the low concentration of the negative ionic species (in corroboration with figure 5.10), the negative ionic species are unable to affect the net electric current density as either their mass (figure 5.4(b)) or their temperature (figure 5.4(d)) are varied in judicious ranges.

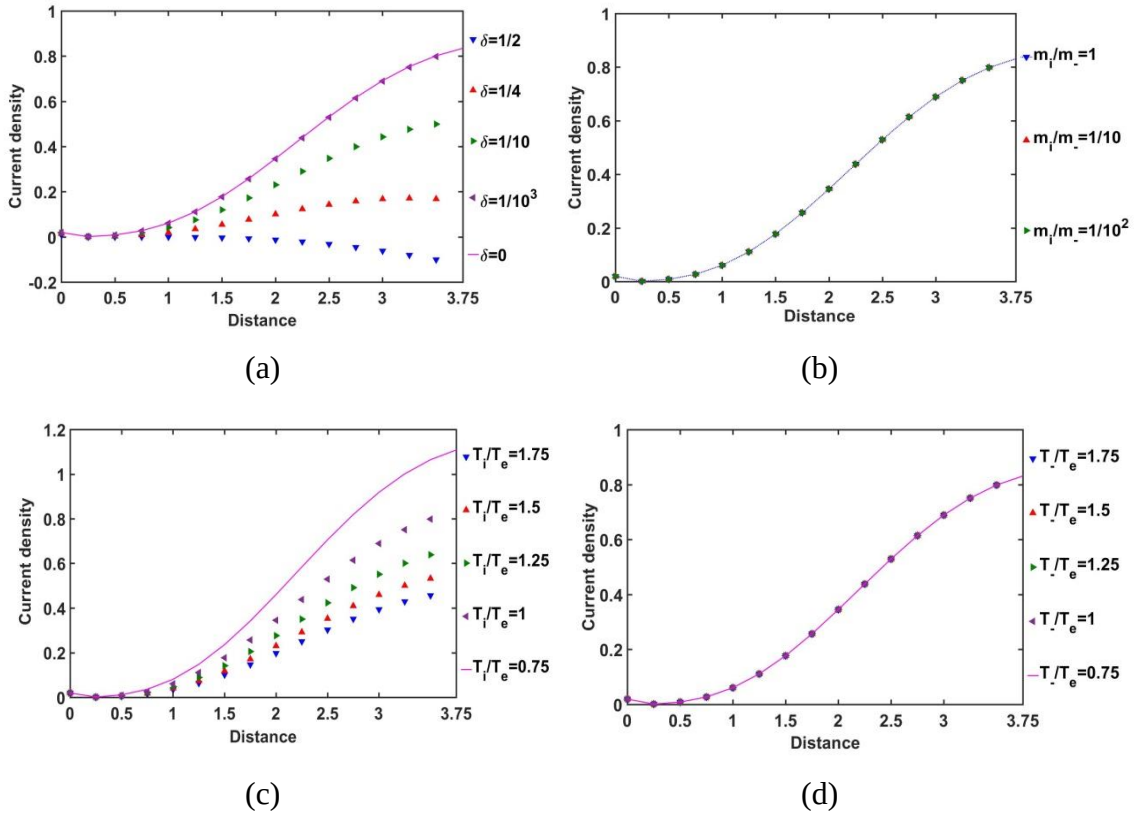

Figure 5.4: *Variation of the SIP current density with the Jeans-normalized heliocentric radial distance for different values of the (a) equilibrium negative-to-positive ion density ratio (δ) with fixed $m_i/m_-=1$, $T_i/T_e=1$ and $T_-/T_e=1$; (b) positive-to-negative ion mass ratio (m_i/m_-) with fixed $\delta=1/1000$, $T_i/T_e=1$ and $T_-/T_e=1$; (c) positive ion-to-electron temperature ratio (T_i/T_e) with fixed $\delta=1/1000$, $m_i/m_-=1$ and $T_-/T_e=1$; and (d) negative ion-to-electron temperature ratio (T_-/T_e) with fixed $\delta=1/1000$, $m_i/m_-=1$ and $T_i/T_e=1$.*

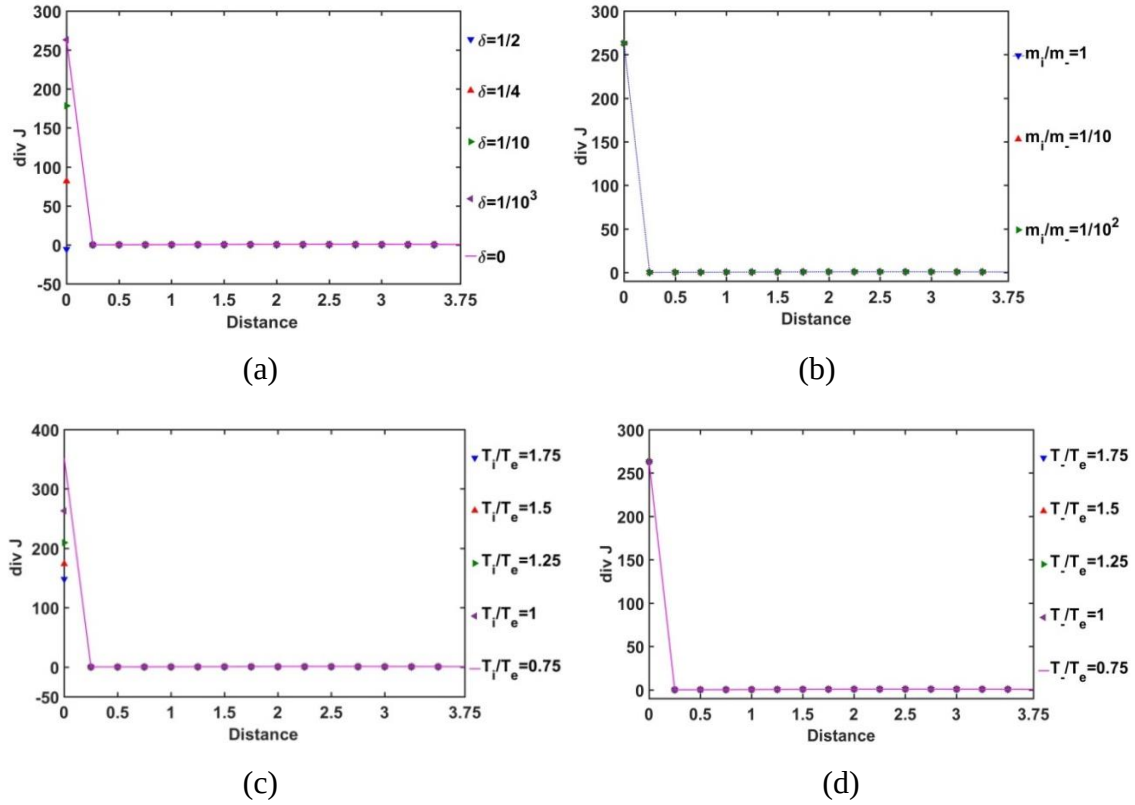

Figure 5.5: *Variation of the divergence of the SIP electric current density (div J) with the Jeans-normalized heliocentric radial distance for different values of the (a) equilibrium negative-to-positive ion density ratio (δ) with fixed $m_i/m_-=1$, $T_i/T_e=1$ and $T_-/T_e=1$; (b) positive-to-negative ion mass ratio (m_i/m_-) with fixed $\delta=1/1000$, $T_i/T_e=1$ and $T_-/T_e=1$; (c) positive ion-to-electron temperature ratio (T_i/T_e) with fixed $\delta=1/1000$, $m_i/m_-=1$ and $T_-/T_e=1$; and (d) negative ion-to-electron temperature ratio (T_-/T_e) with fixed $\delta=1/1000$, $m_i/m_-=1$ and $T_i/T_e=1$. The inner distinctions of these similar profiles obviously lie in the multi-parametric variations of current solar plasma relevance as shown herein.*

In order for exploring the conservative nature of the SIP electric current density, the divergence of the Bohm-normalized SIP current density variation with the Jeans-normalized heliocentric radial distance is depicted in figure 5.5. It is found that the electric current is well conserved throughout the equilibrium SIP, except near the heliocentric region (up to $\xi \approx 0.25$); in particular, no asymptotic variation is noted beyond it (figure 5.5). There exists no local source or sink to affect the net charge production and its directional flow in the SIP, except in the near-heliocentric regions (ξ=0-0.25). The finite non-zero positive divergence of the net electric current density in

the near-heliocentric regions is ascribable to the intense self-gravity action localized in the dense regions, unlike that found in the far-heliocentric regions (ξ > 0.25). The conservative nature of the effective electric current density is interestingly found to be independent of the any of the parametric variations, such as δ, m_i/m_-, T_i/T_e, and T_-/T_e, as considered in our analysis.

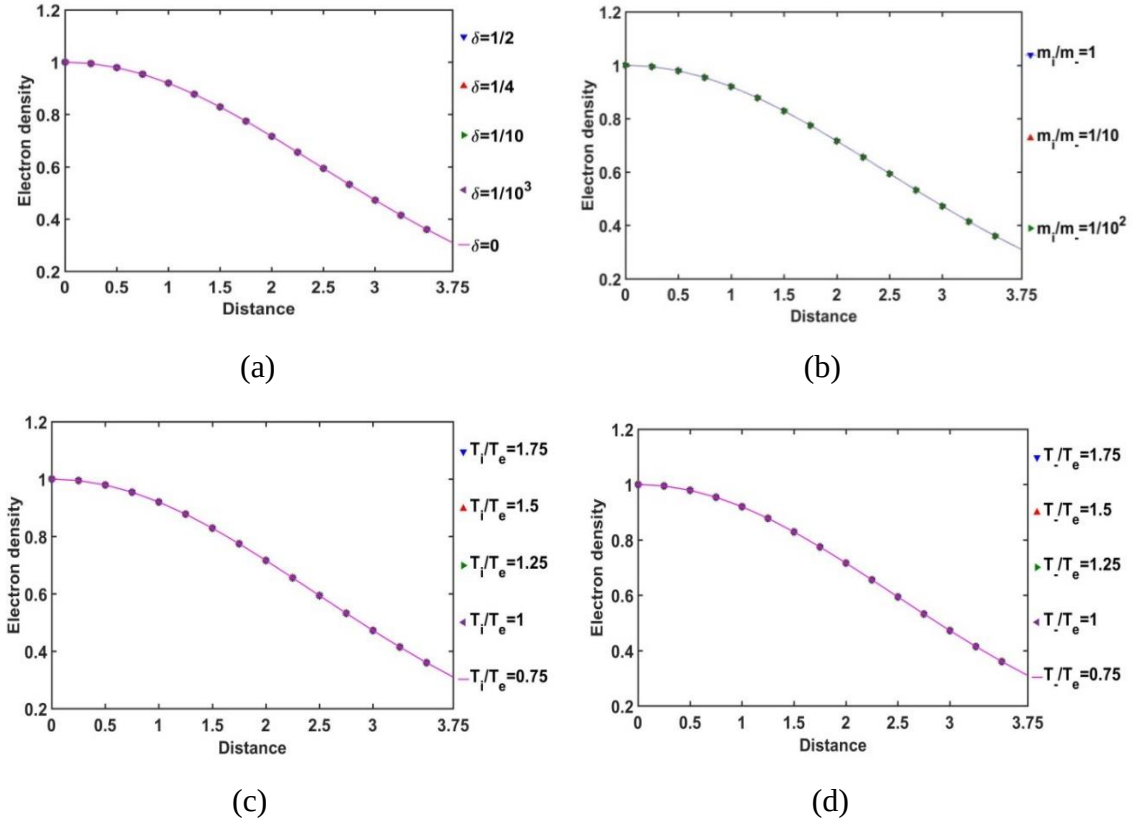

Figure 5.6: *Variation of the normalized SIP electron population density with the Jeans-normalized heliocentric radial distance for different values of the (a) equilibrium negative-to-positive ion density ratio (δ) with fixed $m_i/m_-=1$, $T_i/T_e=1$ and $T_-/T_e=1$; (b) positive-to-negative ion mass ratio (m_i/m_-) with fixed $\delta=1/1000$, $T_i/T_e=1$ and $T_-/T_e=1$; (c) positive ion-to-electron temperature ratio (T_i/T_e) with fixed $\delta=1/1000$, $m_i/m_-=1$ and $T_-/T_e=1$; and (d) negative ion-to-electron temperature ratio (T_-/T_e) with fixed $\delta=1/1000$, $m_i/m_-=1$ and $T_i/T_e=1$. The inner distinctions of these similar profiles obviously lie in the multi-parametric variations of current solar plasma relevance as shown herein.*

The radial variation of the normalized electron population density in the SIP according to the current GES-model equations is portrayed in figure 5.6. It is found that the electron population density is independent of any of the parameters: δ, m_i/m_-, T_i/T_e

and T_-/T_e. The electrons reside mostly in the core and their population density gradually decreases away from the heliocenter. This electron population behaviour is in accordance with the electric potential variation in the SIP (figure 5.2). Away from the heliocenter outwards, the magnitude of the electric potential increases (negative in sense), and hence, the electron population density goes on decreasing to the SSB accordingly. This is quite in accordance with the previous GES-based model predictions [14].

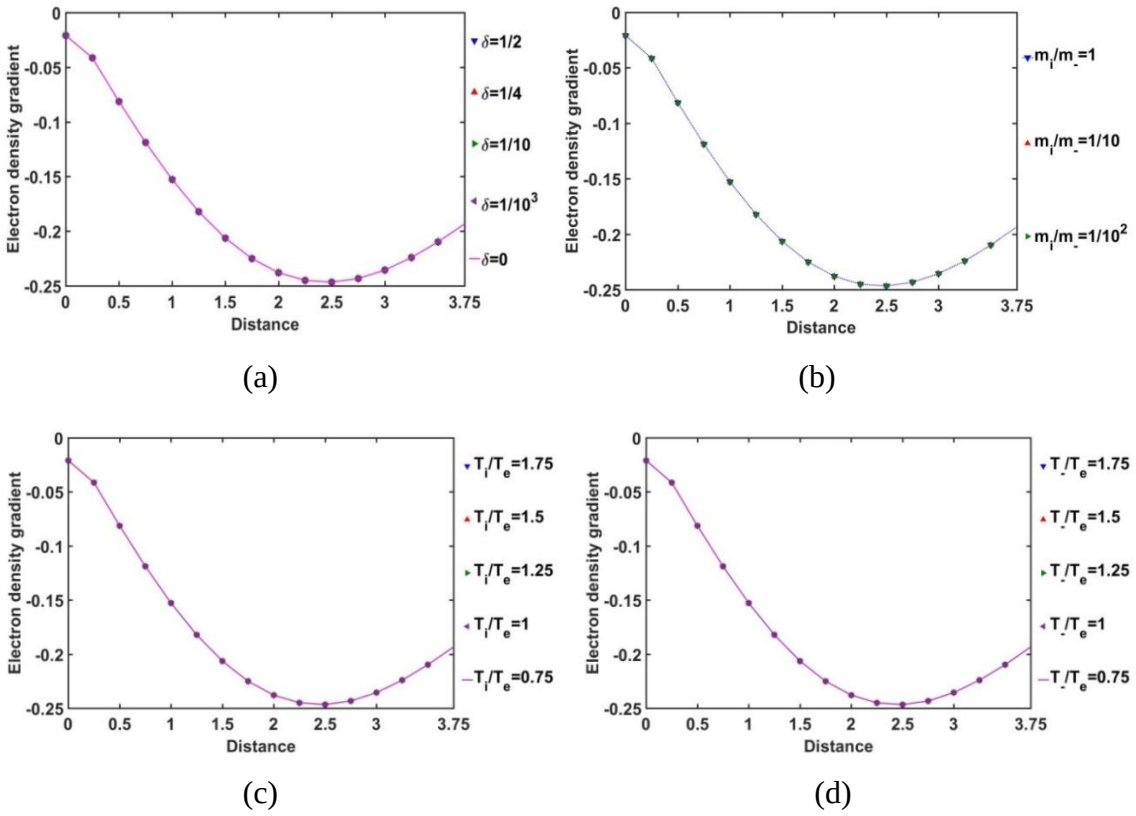

Figure 5.7: *Variation of normalized SIP electron population density gradient with the Jeans-normalized heliocentric radial distance for different values of the (a) equilibrium negative-to-positive ion density ratio (δ) with fixed $m_i/m_-=1$, $T_i/T_e=1$ and $T_-/T_e=1$; (b) positive-to-negative ion mass ratio (m_i/m_-) with fixed $\delta=1/1000$, $T_i/T_e=1$ and $T_-/T_e=1$; (c) positive ion-to-electron temperature ratio (T_i/T_e) with fixed $\delta=1/1000$, $m_i/m_-=1$ and $T_-/T_e=1$; and (d) negative ion-to-electron temperature ratio (T_-/T_e) with fixed $\delta=1/1000$, $m_i/m_-=1$ and $T_i/T_e=1$. The inner distinctions of these similar profiles obviously lie in the multi-parametric variations of current solar plasma relevance as shown herein.*

In figure 5.7, the radial variation of the gradient of the normalized SIP electron population density is illustrated for different considered values of δ (figure 5.7(a)), m_i/m_-

(figure 5.7(b)), T_i/T_e (figure 5.7(c)) and T_-/T_e (figure 5.7(d)). The electron density gradient is found to be negative throughout the entire SIP region. But it reaches to its minimum at ξ=2.5 and then, keeps on increasing slightly towards the SSB. This density gradient behaviour implicates that the electron population density goes on decreasing very sharply (i.e., highly non-uniform radial distribution) away from the heliocenter up to ξ=2.5. This electronic distribution non-uniformity slightly decreases thereafter towards the SSB. Clearly, it has revealed a unique electronic population re-structurization of the SIP modified by the negative ion distribution for the first time in the GES picture.

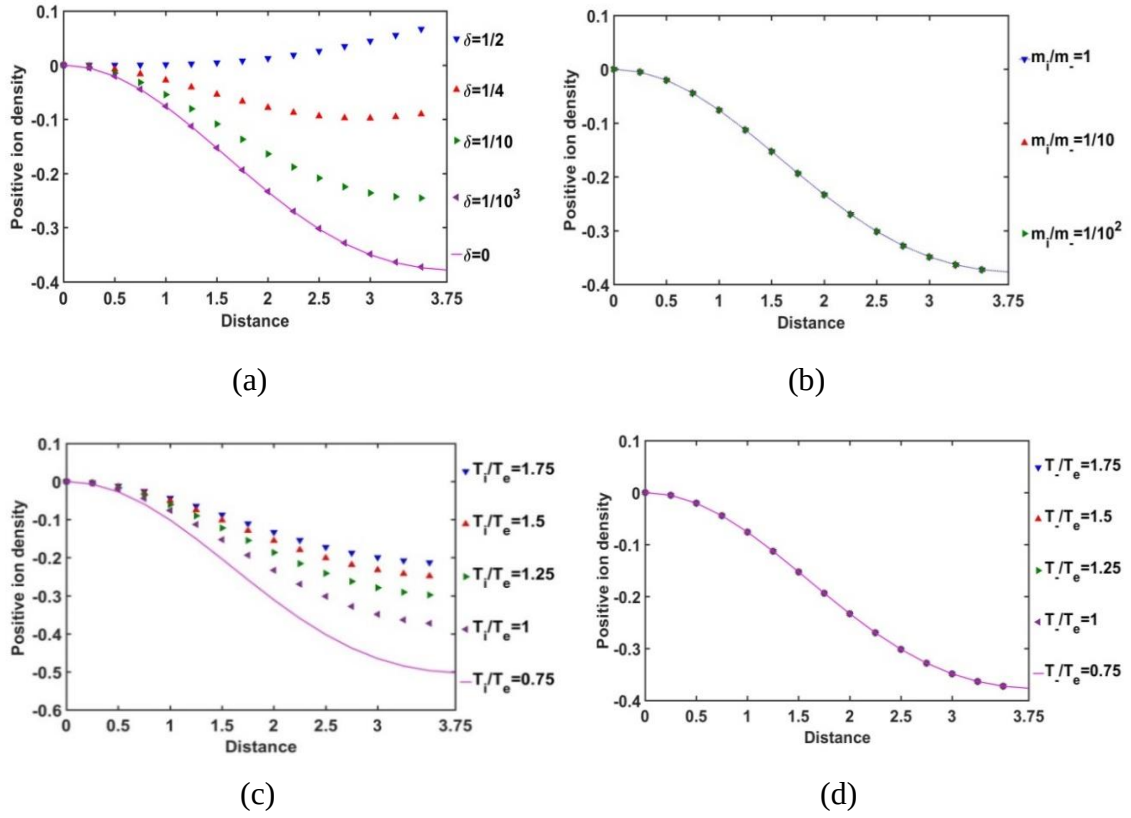

Figure 5.8: *Variation of the SIP positive ion population density with the Jeans-normalized heliocentric radial distance for different values of the (a) equilibrium negative-to-positive ion density ratio (δ) with fixed m_i/m_-=1, T_i/T_e=1 and T_-/T_e=1; (b) positive-to-negative ion mass ratio (m_i/m_-) with fixed δ=1/1000, T_i/T_e=1 and T_-/T_e=1; (c) positive ion-to-electron temperature ratio (T_i/T_e) with fixed δ=1/1000, m_i/m_-=1 and T_-/T_e=1; and (d) negative ion-to-electron temperature ratio (T_-/T_e) with fixed δ=1/1000, m_i/m_-=1 and T_i/T_e=1.*

In figure 5.8, the spatial variation of the normalized positive ion population density in the SIP in the radial direction is presented for different relevant parametric variations. It is revealed herein that the normalized positive ion density is negative in the SIP, except for high δ-values. The negative value of the normalized positive ion population density, however, actually indicates the deficit of positive ion from the average solar plasma density in the equilibrium configuration. As a result, we can infer that the pre-existing quasi-neutrality of the SIP deviates significantly from the normal GES-based solar plasma configuration because of the perturbative negative ions considered afresh. It is further speculating that this positive ionic density variation is sensitive to the equilibrium negative ion concentration (figure 5.8(a)). As the δ-value increases, the negative ion density increases and vice-versa. But the electron density remains the same (figure 5.6(a)). We further see that, with an increase in δ, the normalized positive ion population density deviation in the negative direction decreases from the average plasma density at the equilibrium. This shows that the positive ion density increases in the SIP. The difference in the δ-sensitivities of the positive ion population increases with a decrease in δ and vice-versa. So, the SIP positive ion population saturates itself towards the SIP with the maximum δ-value with increasing δ.

The SIP positive ion density is insensitive to their relative mass with respect to the negative ions (figure 5.8(b)). The relative positive ion temperature with respect to the electron temperature influences the positive ion density commensurably (figure 5.8(c)). It implies that high collision rate and kinetic energy of the positive ions help in their production in the SIP medium. This behaviour saturates itself to high positive ionic temperature SIP-scenario as the difference in the T_i/T_e-sensitivities goes on decreasing with increasing T_i/T_e-value. But the negative ion collisional rate and their kinetic energy do not affect the positive ion population (figure 5.8(d)).

In figure 5.9, the radial variation of the normalized SIP positive ion density gradient is shown for various δ, m_i/m_-, T_i/T_e and T_-/T_e. It is seen that the positive ion density gradient decreases with a decrease in δ and vice-versa (figure 5.9(a)). It depicts that, with a decrease in δ, the positive ion density non-uniformity increases and vice-versa. This gradient sharply falls from the heliocenter to ξ=1.5, which is the location of the maximum non-uniformity; and then keeps on increasing steeply towards the SSB. It is also interestingly found that, the sensitiveness of this non-uniformity on δ becomes more prominent in the radial mid-SIP region than that in the heliocentric and near-SSB regions in the SIP. The difference in the δ-sensitivities of the positive ion density

gradient decreases with an increase in δ and vice-versa. It shows that the increasing negative ion concentration saturates the positive ion density gradient towards the maximum δ-value in the SIP picture (figure 5.9(a)). However, no such sensitive variations are speculated in the case of variation in the positive-to-negative ion mass ratio (figure 5.9(b)). This density gradient behaviour is quite in correlation and consistency with figure 5.8(b) as already explained above.

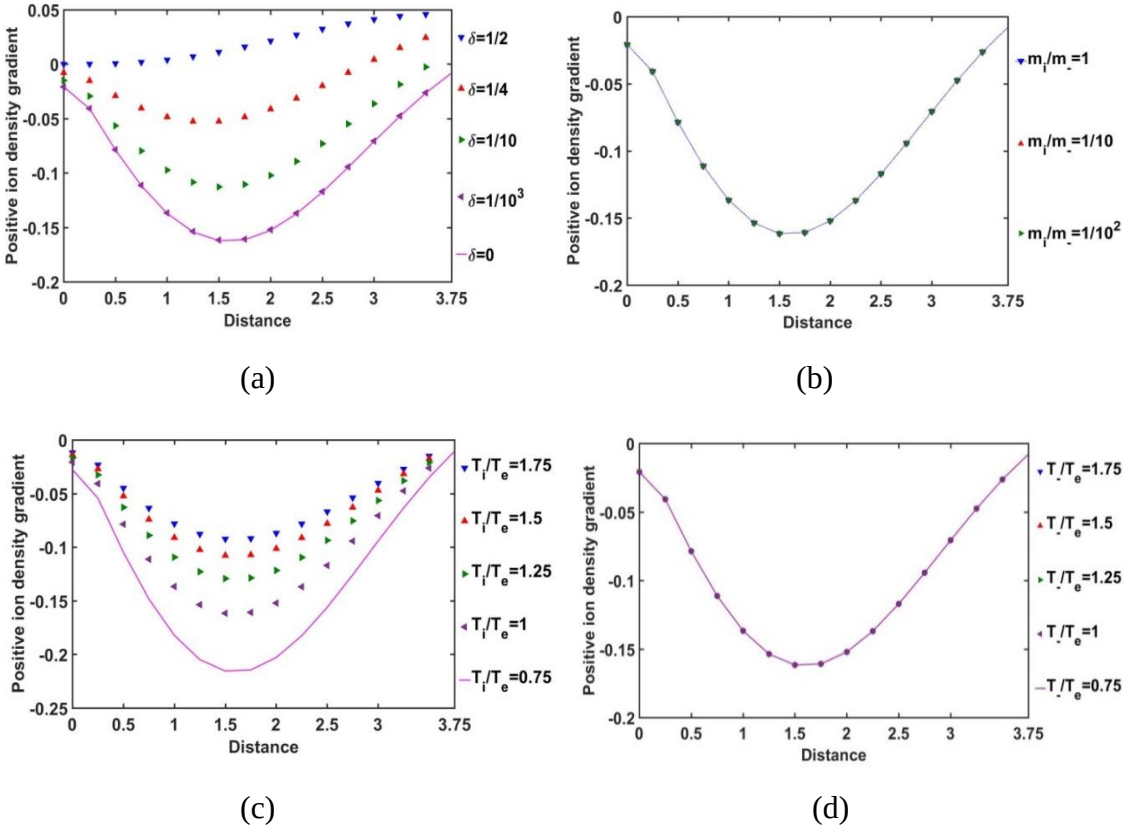

Figure 5.9: *Variation of the normalized SIP positive ion population density gradient with the Jeans-normalized heliocentric radial distance for different values of the (a) equilibrium negative-to-positive ion density ratio (δ) with fixed $m_i/m_-=1$, $T_i/T_e=1$ and $T_-/T_e=1$; (b) positive-to-negative ion mass ratio (m_i/m_-) with fixed $\delta=1/1000$, $T_i/T_e=1$ and $T_-/T_e=1$; (c) positive ion-to-electron temperature ratio (T_i/T_e) with fixed $\delta=1/1000$, $m_i/m_-=1$ and $T_-/T_e=1$; and (d) negative ion-to-electron temperature ratio (T_-/T_e) with fixed $\delta=1/1000$, $m_i/m_-=1$ and $T_i/T_e=1$.*

As depicted in figure 5.9(c), we see that the positive ion density gradient decreases with a decrease in the positive ion temperature with respect to the electronic temperature and vice-versa. For a high positive ionic temperature, their population

density uniformity increases in the SIP medium. This density behaviour may be attributable to the high kinetic energy and collision rate of the positive ions that may facilitate in their rapid production in the SIP medium causing high population density uniformity (figure 5.8(c)). The positive ion density gradient saturates itself towards the SIP configuration with a high positive ion temperature, as the difference in the T_i/T_e-sensitivities goes on decreasing with an increase in the T_i/T_e-value. It is quite in accordance with the basic physical insights as already discussed in case of figure 5.8(c); and so forth. This spatial variation of the positive ionic density gradient is quite insensitive to the negative ion-to-electron temperature ratio, as clearly evident from figure 5.9(d), and so forth. This behaviour is again quite valid with that in figure 5.8(d).

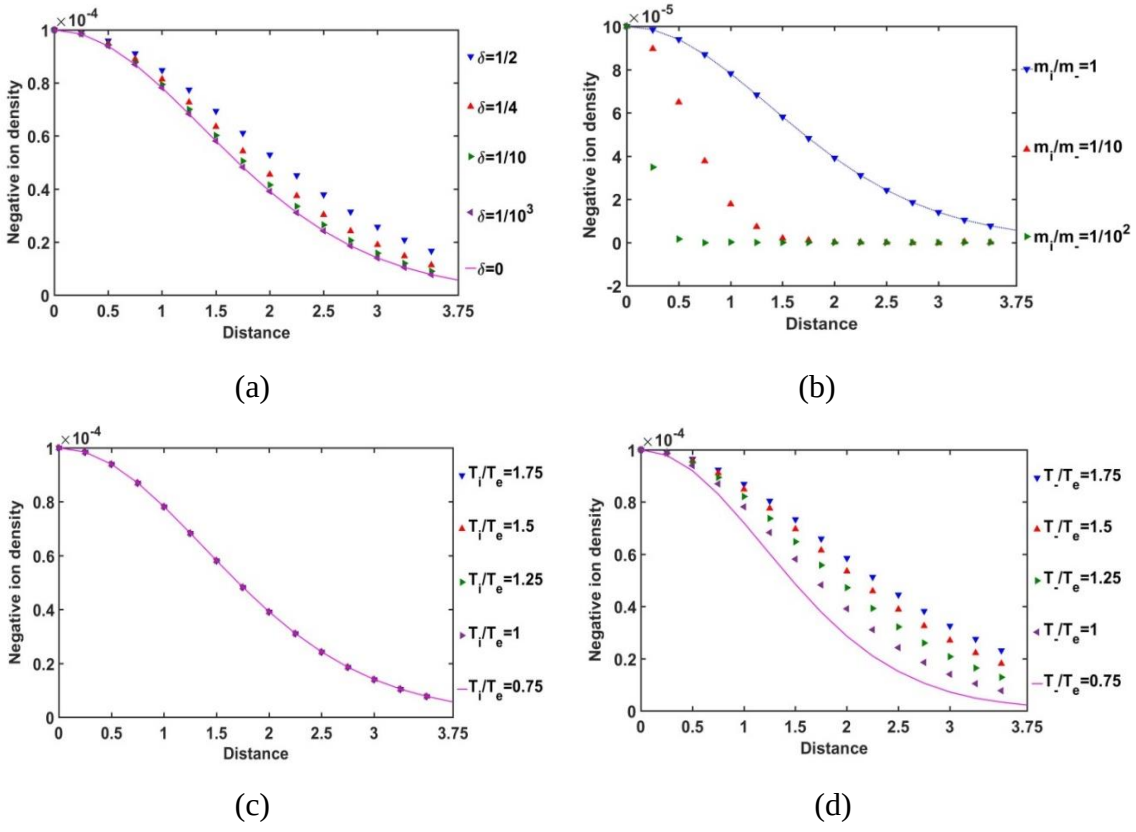

Figure 5.10: *Variation of the SIP negative ion population density with the Jeans-normalized heliocentric radial distance for different values of the (a) equilibrium negative-to-positive ion density ratio (δ) with fixed $m_i/m_-=1$, $T_i/T_e=1$ and $T_-/T_e=1$; (b) positive-to-negative ion mass ratio (m_i/m_-) with fixed $\delta=1/1000$, $T_i/T_e=1$ and $T_-/T_e=1$; (c) positive ion-to-electron temperature ratio (T_i/T_e) with fixed $\delta=1/1000$, $m_i/m_-=1$ and $T_-/T_e=1$; and (d) negative ion-to-electron temperature ratio (T_-/T_e) with fixed $\delta=1/1000$, $m_i/m_-=1$ and $T_i/T_e=1$.*

The radial variations of the normalized SIP negative ion population density for δ, m_i/m_-, T_i/T_e and T_-/T_e –variations are graphically depicted in figure 5.10. It is found that the negative ion density in the SIP medium increases with an increase in δ and vice-versa (figure 5.10(a)). We interestingly notice that some residual negative ions are still present in the SIP even for the δ=0 case. These residual negative ionic effects may be ascribable to the diverse cosmic non-ideality influences causing local ionization, recombination, etc. [11]. The difference in the δ-sensitivities of the negative ion population density decreases with a decrease in the δ-value. So, the negative ion population saturates itself in the SIP with decrease in δ to the δ=0 SIP scenarios.

It is furthermore found that the negative ion population is highly sensitive to the positive-to-negative ion mass ratio (figure 5.10(b)). With an increase in the negative ionic mass, their population density falls rapidly in the SIP. Hence, it is hereby revealed that the SIP medium is not favourable for the heavy clustered negative ion formation, for the first time. It is worth mentioning here that this negative ion population behaviour is following the observational evidence that the hydrogen ion (H^-) accounts for the large part of the continuous absorption of the solar atmosphere. However, other heavier negative ions have been detected later with advancement in the spectrophotometric analytical techniques, as already mentioned earlier [5, 6]. Hence, this match between the current theoretical findings by us and the previous observational scenarios by others enhances the relevance and reliability of our present investigation significantly.

The negative ion population density is insensitive to the positive ion-to-electron temperature ratio (figure 5.10(c)). So, the high positive ionic temperature and hence, collision does not influence in the production of negative ions in the SIP.

Besides, the negative ion population density is influenced significantly by the negative ion-to-electron temperature ratio effectively (figure 5.10(d)). So, high negative ionic temperature and hence, high kinetic energy and collision help in the generation of the negative ionic species in the SIP. It is also interestingly noticed that the difference in the T_-/T_e-sensitivities decreases with an increase in the T_-/T_e-value and vice-versa. So, the negative ion density saturates itself towards their high temperature SIP-scenarios with an increase in their temperature with respect to the electronic temperature. It is also interestingly found that this T_-/T_e-sensitivity become more prominent away from the heliocenter towards the SSB (figure 5.10(d)).

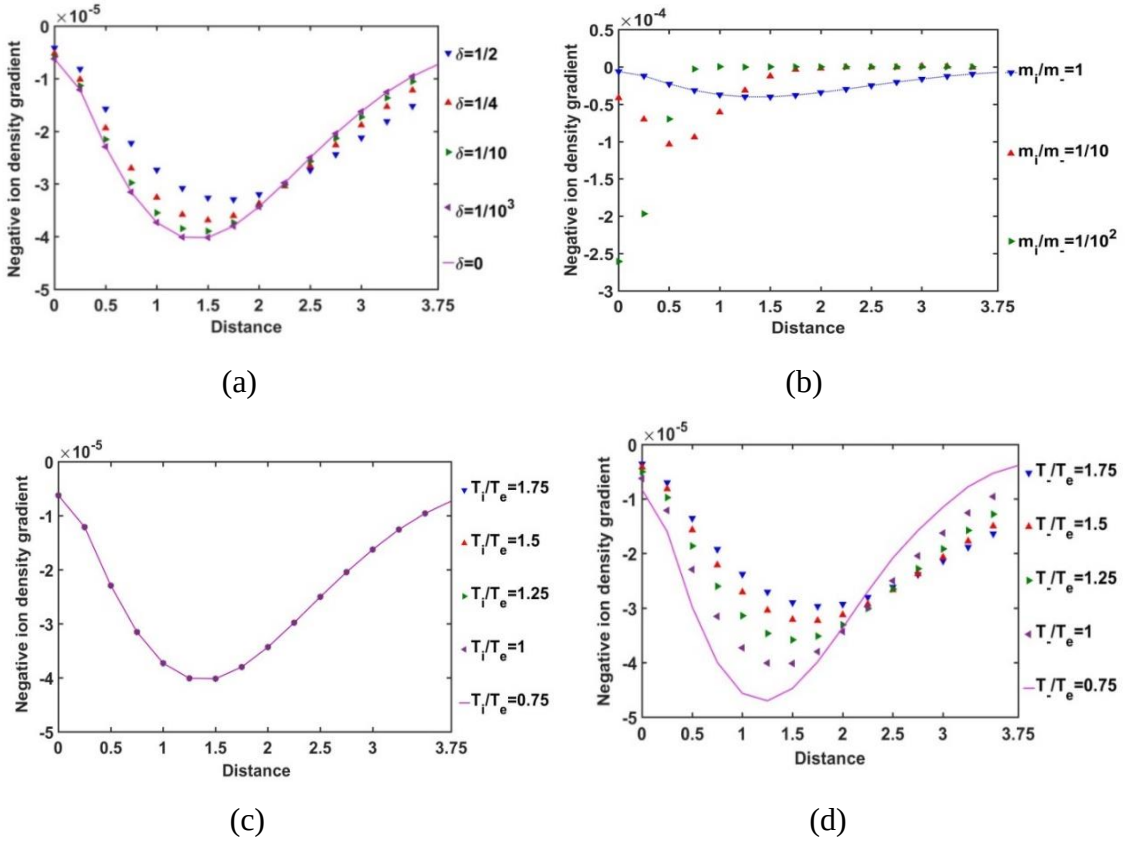

Figure 5.11: *Variation of the normalized SIP negative ion population density gradient with the Jeans-normalized heliocentric radial distance for different values of (a) equilibrium negative-to-positive ion density ratio (δ) with fixed $m_i/m_-=1$, $T_i/T_e=1$ and $T_-/T_e=1$; (b) positive-to-negative ion mass ratio (m_i/m_-) with fixed $\delta=1/1000$, $T_i/T_e=1$ and $T_-/T_e=1$; (c) positive ion-to-electron temperature ratio (T_i/T_e) with fixed $\delta=1/1000$, $m_i/m_-=1$ and $T_-/T_e=1$; and (d) negative ion-to-electron temperature ratio (T_-/T_e) with fixed $\delta=1/1000$, $m_i/m_-=1$ and $T_i/T_e=1$.*

In figure 5.11, the variation of the normalized SIP negative ion density gradient with the Jeans-normalized heliocentric radial distance is shown for different values of δ, m_i/m_-, T_i/T_e and T_-/T_e. It is seen that the uniformity in the negative ion population density decreases with an increase in the radial distance up to $\xi \approx 1.5$ and then keeps on increasing subsequently towards the SSB for various δ-values (figure 5.11(a)). It is interestingly seen that there lies a radial location between ξ=2 - 2.5, where this density gradient becomes the same irrespective of the δ-values, and the variation trend becomes reverse afterwards to the SSB. So, there appears a δ-insensitive location, which may be termed as a trans-critical point, for the negative ion population non-uniformity in the SIP. The δ-sensitivity of the negative ion density gradient goes on decreasing with a decrease

in the δ-value. Therefore, this density gradient saturates itself towards the δ=0 case as δ decreases in the SIP configuration.

It is furthermore seen that the non-uniformity in the negative ion population density in the SIP is higher for the heavier negative ions; particularly, in the near-heliocentric region, and becomes insignificant away from the heliocenter (figure 5.11(b)). This is because of the fact that the negative ion population in such off-centric region becomes considerably negligible as seen previously in figure 5.10(b). Thus, the negative ion density gradient evolves in accordance with the usual plasma collective interaction processes as already discussed above. This spatial variation of the density gradient is insensitive to the positive ion-to-electron temperature ratio, as evident from figure 5.11(c). This behaviour is again quite in fair conformity with figure 5.10(c).

It is speculated from figure 5.11(d) that the negative ion density gradient decreases with a decrease in the negative ion temperature with respect to the electronic temperature. For high negative ionic temperature, their population density uniformity increases in the SIP medium. This behaviour may be attributable to the kinetic energy and high collision rate of the negative ions that may help in their production in the SIP medium. As a consequence, it causes high population uniformities in the SIP (figure 5.10(d)). The negative ion density gradient saturates itself towards the SIP-picture with high negative ion temperature, as the difference in the T_-/T_e-sensitivities goes on decreasing with an increase in the T_-/T_e – value. This trend is evidently in accordance with the basic physical mechanisms already stated in figure 5.10(d). It is noteworthy that the trans-critical point on the T_-/T_e-sensitivity here (figure 5.11(d)), similar to that on the δ-sensitivity (figure 5.11(a)), lies in the same region bounded between ξ=2 - 2.5.

In figure 5.12, we depict the normalized population density profile of the SIP constituent species in a conjoint pattern. It is interestingly noticed that the profile of the negative ion population density with variation of the electronic and positive ionic population density follows a particular trail for each δ to meet the maximum value of the negative ionic density. This maximum density value is found to be the same irrespective of the δ-values (figure 5.12(a)). As already explained before (figure 5.10(a)), we can identify that the vertex of the trails meaning the negative ion population density at the heliocenter. The density declining trend along the trails shows the population of the constituents as seen by an observer from the heliocenter towards the SSB. The difference in the δ-sensitivities of the trailing patterns becomes more prominent towards the lower δ-values than that seen in the higher δ-corners. This happens as a result of saturation of

the plasma constituents in the SIP towards the maximum δ-SIP scenarios with an increase in the δ-value, and so forth.

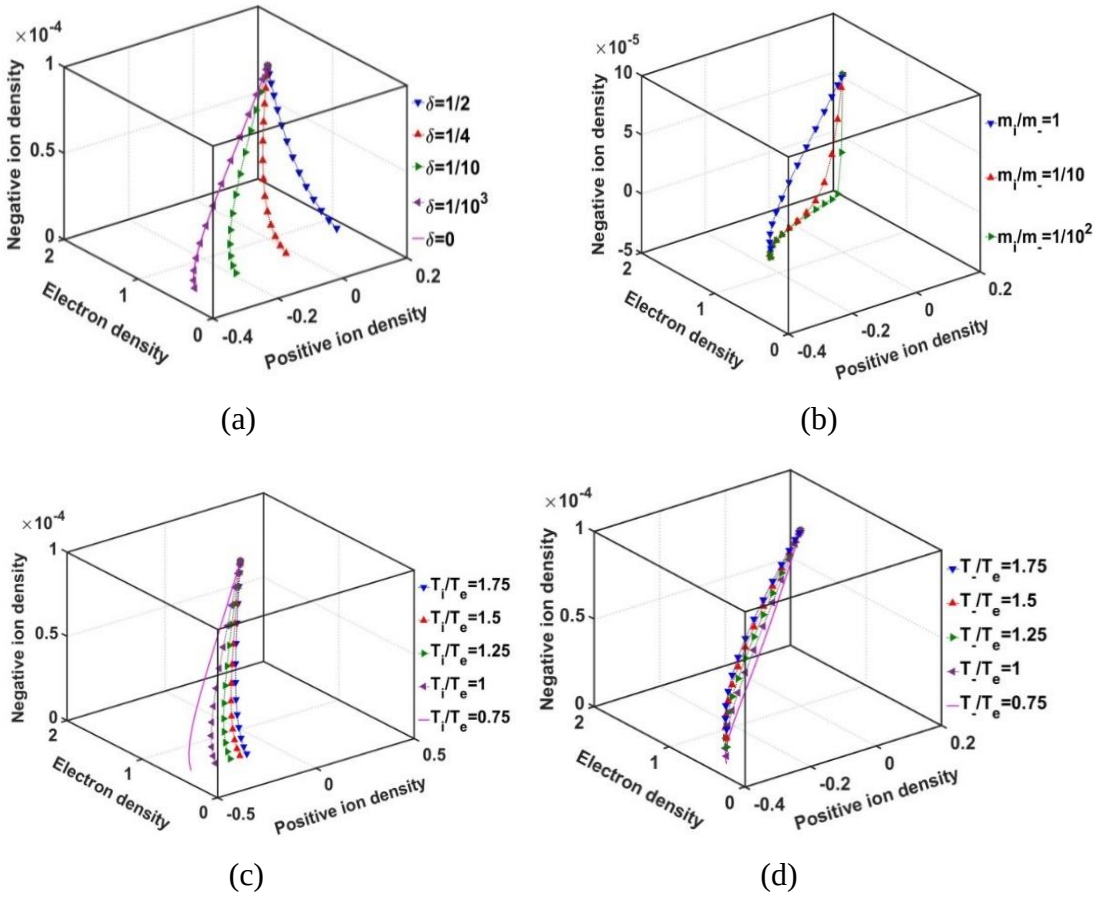

Figure 5.12: *Variation of the negative ion population density with the positive ion and electron population densities in the SIP for different values of the (a) equilibrium negative-to-positive ion density ratio (δ) with fixed $m_i/m_-=1$, $T_i/T_e=1$ and $T_-/T_e=1$; (b) positive-to-negative ion mass ratio (m_i/m_-) with fixed $\delta=1/1000$, $T_i/T_e=1$ and $T_-/T_e=1$; (c) positive ion-to-electron temperature ratio (T_i/T_e) with fixed $\delta=1/1000$, $m_i/m_-=1$ and $T_-/T_e=1$; and (d) negative ion-to-electron temperature ratio (T_-/T_e) with fixed $\delta=1/1000$, $m_i/m_-=1$ and $T_i/T_e=1$.*

As in figure 5.12(b), we find the appearance of a common vertex of the negative ion density trails irrespective of the positive-to-negative ionic mass ratio. This vertex region represents the negative ion density near the $\zeta \approx 0$ regions. The difference in the m_i/m_--sensitivities of the trail become less prominent with an increase in the negative ionic mass as the formation of the heavy negative ions is not favoured in the SIP medium (figure 5.10(b)). The downward movement along the trail corresponds to the solar

plasma constituent's density encountered in moving away from the heliocenter towards the SSB. This off-centric declining trend of the SIP constituents is fairly in accord with the basic physical insights already developed from the study of figure 5.10(b).

In a similar way, from figure 5.12(c), we see the appearance of a common vertex of the negative ion density trail irrespective of the positive ion-to-electron temperature ratio. The vertex corresponds to the negative ion population density near the $\xi \approx 0$ regions. The difference in the T_i/T_e-sensitivities of the trails becomes less prominent with higher T_i/T_e-values. This behaviour of the trail is attributable to the property discussed in case of studying figure 5.8(c). The downward movement along the trails corresponds to the plasma constituent density as encountered by an observer in moving away from the heliocenter towards the SSB (in agreement with figure 5.10(c)).

We see further, as in figure 5.12(d), the appearance of a common vertex of the negative ion density trails irrespective of the negative ion-to-electron temperature ratio, which corresponds to the population density near the $\xi \approx 0$ regions, as already found in the previous cases as well (figures 5.12(a)-5.12(c)). The difference in the T_-/T_e-sensitivities of the trails becomes less prominent with higher T_-/T_e-values. This behaviour of the trail is attributable to the property discussed in studying figure 5.10(d). The downward movement along the trails corresponds to the constituent population density encountered in moving away from the heliocenter towards the SSB (as clearly depicted in figure 5.10(d) as well). As a consequence, we can draw a common conclusive remark from the above discussion that the heliocentric density of the constituent species is absolutely the same irrespective of the variations in the input constitutive characteristic parameters, such as δ, m_i/m_-, T_i/T_e and T_-/T_e (figures 5.12(a)-5.12(d)).

In figures 5.13-5.16, the colour-spectral profiles of the normalized positive ion population density variation with the negative ion and electron population densities in the SIP are depicted for the fulfilment of the pre-existing equilibrium plasma quasi-neutrality condition. These profiles reveal the basic realistic spatial plasma evolutionary behaviours when compared with the actual constituent population density profiles as in figure 5.6, figure 5.8, figure 5.10, and figure 5.12. These colour phase maps are obtained by numerically simulating the SIP electrostatic Poisson equation (equation 5.18) with the consideration of negligible left hand side magnitude due to the presence of $\lambda_{De}/\lambda_J \sim 10^{-20}$. The judicious SIP input and initial parametric values are already discussed previously. It is worth mentioning that the λ_{De}/λ_J -value signifies a closeness

to non-neutral plasma approximation ($\lambda_{De}/\lambda_J \to 0$ signifies electrical neutrality; otherwise, non-neutrality).

It is found from figure 5.13 that the positive ion population density is highly sensitive to the δ-value in maintaining the said equilibrium plasma quasi-neutrality in the SIP. With a decrease in the δ-value, the positive ion density increases significantly towards the highest electron density corner and vice-versa (i.e., towards the heliocentric region as it is clear from figure 5.6). However, in reality, it is seen from figure 5.8(a) and figure 5.12(a) that the positive ion density approaches negligible value towards the heliocenter. So, the medium deviates from the equilibrium plasma quasi-neutrality in the heliocenter. This deviation increases with a decrease in the δ-value as it is clear from figure 5.13. It is also noticed from figure 5.8(a) that as one moves away from the heliocenter towards the SSB, and also with a decrease in the δ-value, the positive ion population density takes increasingly negative magnitude. So, it can be inferred, interestingly, that the SIP medium structurizes itself in such a way that its deviation from the equilibrium solar plasma quasi-neutrality increases with an increase in the radial distance as well as a decrease in the δ-value.

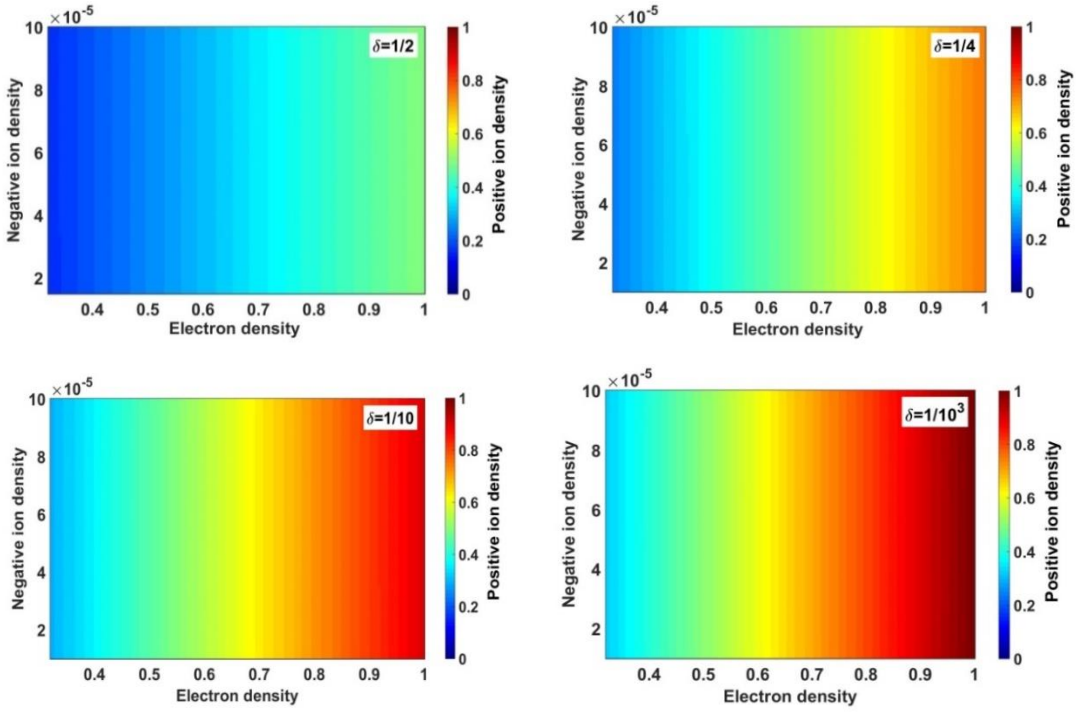

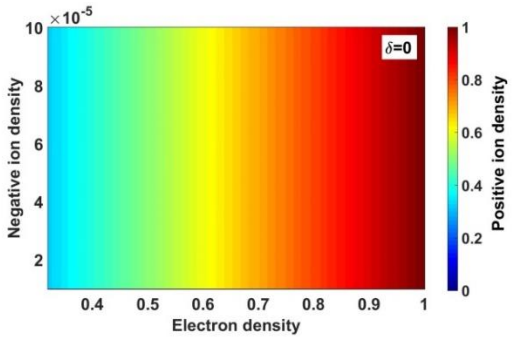

Figure 5.13: *Variation of the negative ion population density with the positive ion and electron population densities in the SIP for different values of the equilibrium negative-to-positive ion density ratio (δ) with fixed $m_i/m_-=1$, $T_i/T_e=1$ and $T_-/T_e=1$ as per the equilibrium solar plasma quasi-neutrality condition.*

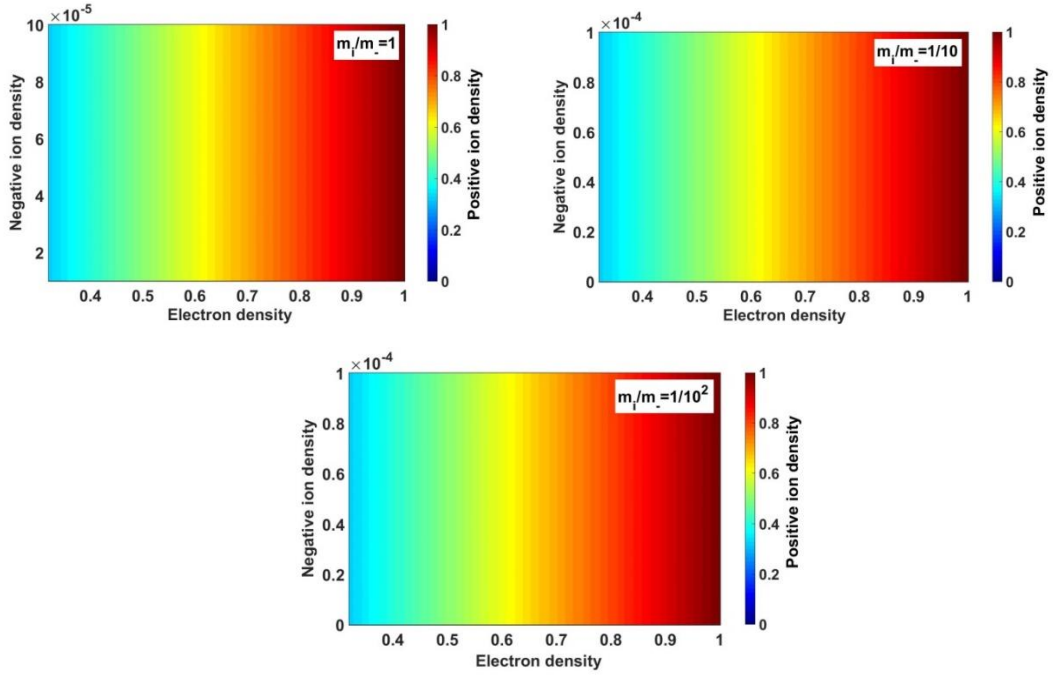

Figure 5.14: *Variation of the negative ion population density with the positive ion and electron population densities in the SIP for different values of the positive-to-negative ion mass ratio (m_i/m_-) with fixed $\delta=1/1000$, $T_i/T_e=1$ and $T_-/T_e=1$ as per the plasma quasi-neutrality condition.*

It is seen from figure 5.14 that the positive ion, negative ion, and the electron population densities are insensitive to the m_i/m_--variation for maintaining the equilibrium plasma quasi-neutrality in the SIP. In reality, although this colour-spectral pattern is in accordance with figure 5.8(b), but it is against figure 5.10(b). It is seen from figure 5.10(b) and figure 5.12(b) that the negative ion population density is dependent on the

m_i/m_--value. In fact, the heavy negative ion formation is not favoured in the SIP medium. Hence, figure 5.14 clearly displays the realistic SIP deviation from local quasi-neutral equilibrium plasma behaviour.

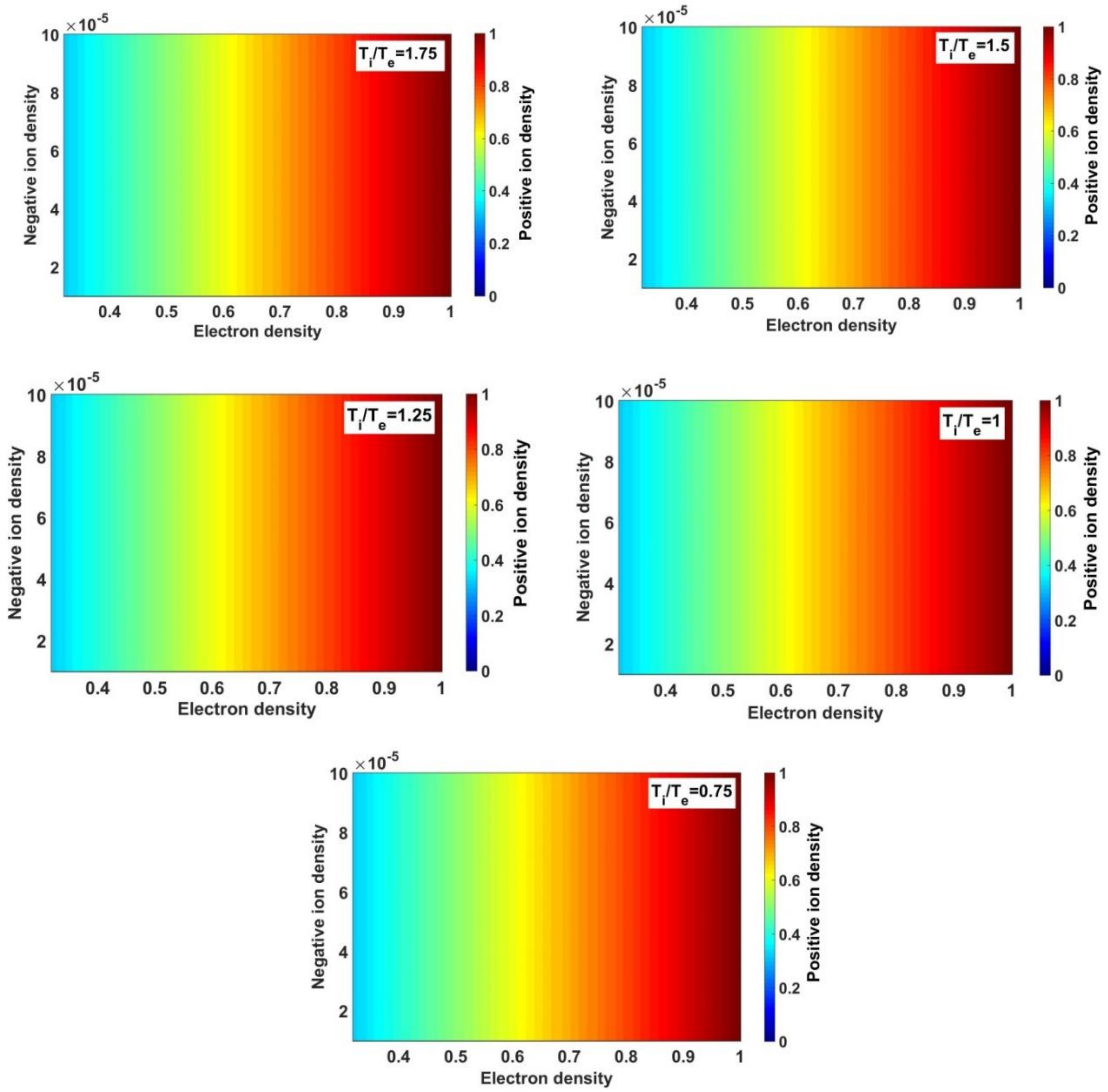

Figure 5.15: *Variation of the negative ion population density with the positive ion and electron population densities in the SIP for different values of the positive ion-to-electron temperature ratio (T_i/T_e) with fixed δ=1/1000, m_i/m_-=1 and T_-/T_e=1 as per the local quasi-neutrality condition.*

It is clear from figure 5.15 that the positive and negative ion population densities are insensitive to the T_i/T_e-variation for maintaining the equilibrium plasma quasi-neutrality in the SIP. In fact, it is against figure 5.8(c) and figure 5.12(c); though it is in accordance with figure 5.6(c) and figure 5.10(c). It is seen from figure 5.8(c) that the

positive ion population density is dependent on the T_i/T_e-value and hence, there appear separate trails in figure 5.12(c) for different T_i/T_e-variational cases. Hence, this profile (figure 5.15) clearly portrays the realistic SIP deviation from the said equilibrium configuration.

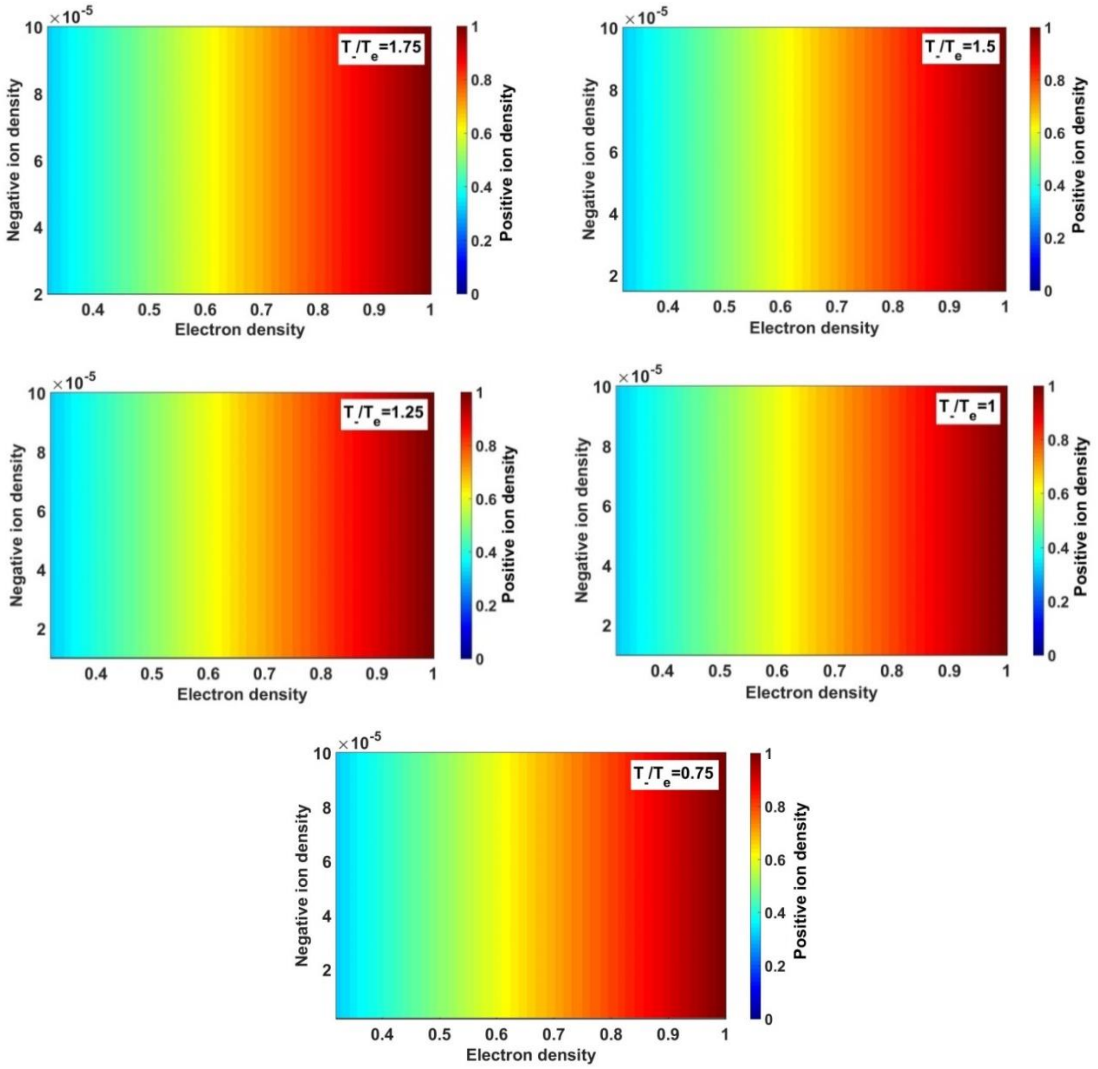

Figure 5.16: *Variation of the negative ion population density with the positive ion and electron population densities in the SIP for different values of the negative ion-to-electron temperature ratio (T_-/T_e) with fixed $\delta=1/1000$, $m_i/m_-=1$ and $T_i/T_e=1$ as per the local quasi-neutrality condition.*

It is noticeable from figure 5.16 that the positive and negative ion population densities are insensitive to the T_-/T_e-variation for maintaining the equilibrium SIP quasi-neutrality condition. It is noteworthy that it is against figure 5.10(d) and figure 5.12(d); though it is in accordance with figure 5.6(d) and figure 5.8(d). We see from figure

5.10(d) that the negative ion population density is dependent on the T_-/T_e-value and hence, there appear separate trails in figure 5.12(d) for different T_-/T_e-variational cases. Consequently, this profile (figure 5.16) clearly shows the realistic SIP deviational nature with respect to the said idealistic local plasma quasi-neutrality condition.

5.3.2 SWP-illustration

To explore the equilibrium SWP behaviours, its various relevant properties are studied numerically with the help of the normalized SWP governing equations (equations (5.30)-(5.38)). In figure 5.17, the radial variations of the normalized SWP electric potential from the SSB to 1 au for δ, m_i/m_-, T_i/T_e and T_-/T_e-variations are shown. Here, the spatial grid size used is 40. For plotting the profiles, we have considered $T_{i(-)}/T_e$ = 1.25. The reason behind is that the Mach number in the SWP turns supersonic for $T_i/T_e > 1$ (figure 5.18). So, keeping in mind the observed supersonic nature of the solar wind particles, the rest of the profiles are structured for T_i/T_e = 1.25, which is the considered smallest value for which supersonic Mach number results. This assumption of $T_{i(-)}/T_e > 1$ is quite fair in line with diverse solar observations, as clearly depicted in S. No. 5 of Table 5.4. It is found that the SWP electric potential is insensitive to any of the above-mentioned parametric variations. The SWP electric potential is insignificant in the near-SSB region as compared to the far-SSB region in the SWP medium. It signifies high material concentration in the near SSB-zone. It results in a high degree of shielding effect between the opposite-polarity plasma species. Away from the SSB, the material concentration decreases and due to increase in diffusivity of the SWP constituents, the electrostatic effects become more significant. This result on the constitutive electrostatic response characteristics is fairly in accord with the recently reported thermo-statistically modified solar-picture based on the realistic GES-model formalism [14].

As portrayed in figure 5.18, the spatial variation of the SWP positive ion Mach number from the SSB up to 1 au is depicted for different values of δ (figure 5.18(a)), m_i/m_- (figure 5.18(b)), T_i/T_e (figure 5.18(c)) and T_-/T_e (figure 5.18(d)). It is interestingly found that there is an abrupt subsonic-to-supersonic transition of the positive ion Mach number for $T_i/T_e \geq 1$ just outside the SSB (figure 5.18(c)). The low density of the SWP medium facilitates the high positive ionic velocity in contrast to the dense SIP medium case as already seen in figure 5.3. This is fairly in agreement with the basic principle of the well-known Newtonian acoustics, as seen extensively in the earlier GES-scenarios as

well. It is because of the fact that the bulk plasma flow occurs at the phase speed of the bulk (ion) acoustic mode, and so forth [7].

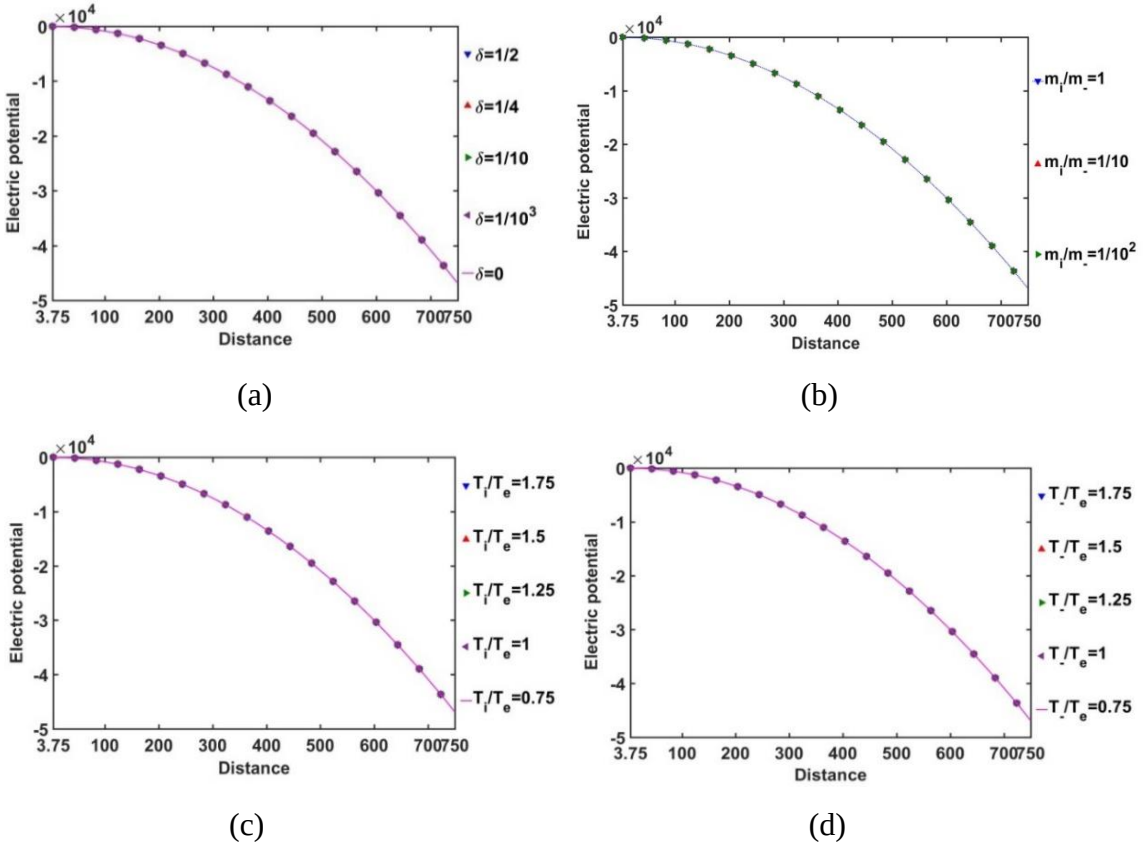

Figure 5.17: *Variation of the normalized SWP electric potential with the Jeans-normalized heliocentric radial distance for different values of the (a) equilibrium negative-to-positive ion density ratio (δ) with fixed $m_i/m_-=1$, $T_i/T_e=1.25$ and $T_-/T_e=1.25$; (b) positive-to-negative ion mass ratio (m_i/m_-) with fixed δ=1/1000, $T_i/T_e=1.25$ and $T_-/T_e=1.25$; (c) positive ion-to-electron temperature ratio (T_i/T_e) with fixed δ=1/1000, $m_i/m_-=1$ and $T_-/T_e=1.25$; and (d) negative ion-to-electron temperature ratio (T_-/T_e) with fixed δ=1/1000, $m_i/m_-=1$ and $T_i/T_e=1.25$, as per the recent solar observational reports. The inner distinctions of these similar profiles obviously lie in the multi-parametric variations of current solar plasma relevance as shown herein.*

The Mach number is highly sensitive to the positive ion-to-electron temperature ratio (T_i/T_e), as clearly evident in figure 5.18(c). It is interestingly noticed that the sonic transition location on the heliocentric radial space shifts away from the SSB outwards with an increase in the T_i/T_e-value and vice-versa. The Mach number is of the order of unity for T_i/T_e=1. In other words, the positive ion velocity reaches the order of magnitude

of the average sound speed in the SIP. With an increase in T_i/T_e-value, the Mach number increases and vice-versa. So, high positive ionic temperature helps the ions to attain a high velocity in the rare SWP.

It is noteworthy here that the magnitude of the solar wind speed, as already obtained from various solar observational missions, is supersonic in nature [8]. So, for such a high-speed scenario, a non-isothermal plasma medium is clearly suggested by our presented model formalism, in accordance with the realistic picture [14, 16]. The consistency of this SWP Mach number behaviour with previously reported observations further strengthens the reliability of our proposed calculation scheme. We find throughout that the SWP Mach number at a distance of 1 au comes out approximately to be M_{1au}=1.13 (figure 5.18). This supersonic SWP flow dynamics is quite in accordance with previously reported results [7].

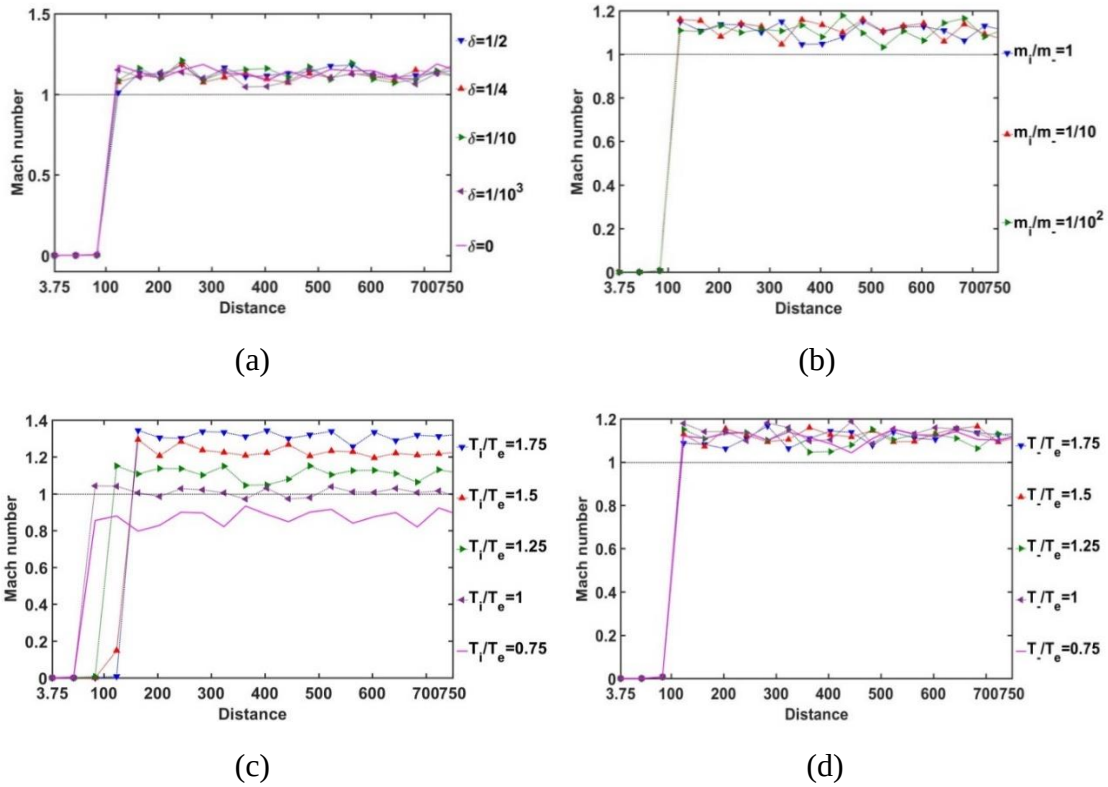

Figure 5.18: *Variation of SWP Mach number with Jeans-normalized heliocentric radial distance for different values of (a) equilibrium negative-to-positive ion density ratio (δ) with fixed m_i/m_-=1, T_i/T_e=1.25 and T_-/T_e=1.25; (b) positive-to-negative ion mass ratio (m_i/m_-) with fixed δ=1/1000, T_i/T_e=1.25 and T_-/T_e=1.25; (c) positive ion-to-electron temperature ratio (T_i/T_e) with fixed δ=1/1000, m_i/m_-=1 and T_-/T_e=1.25; and (d) negative ion-to-electron temperature ratio (T_-/T_e) with fixed δ=1/1000, m_i/m_-=1 and T_i/T_e=1.25.*

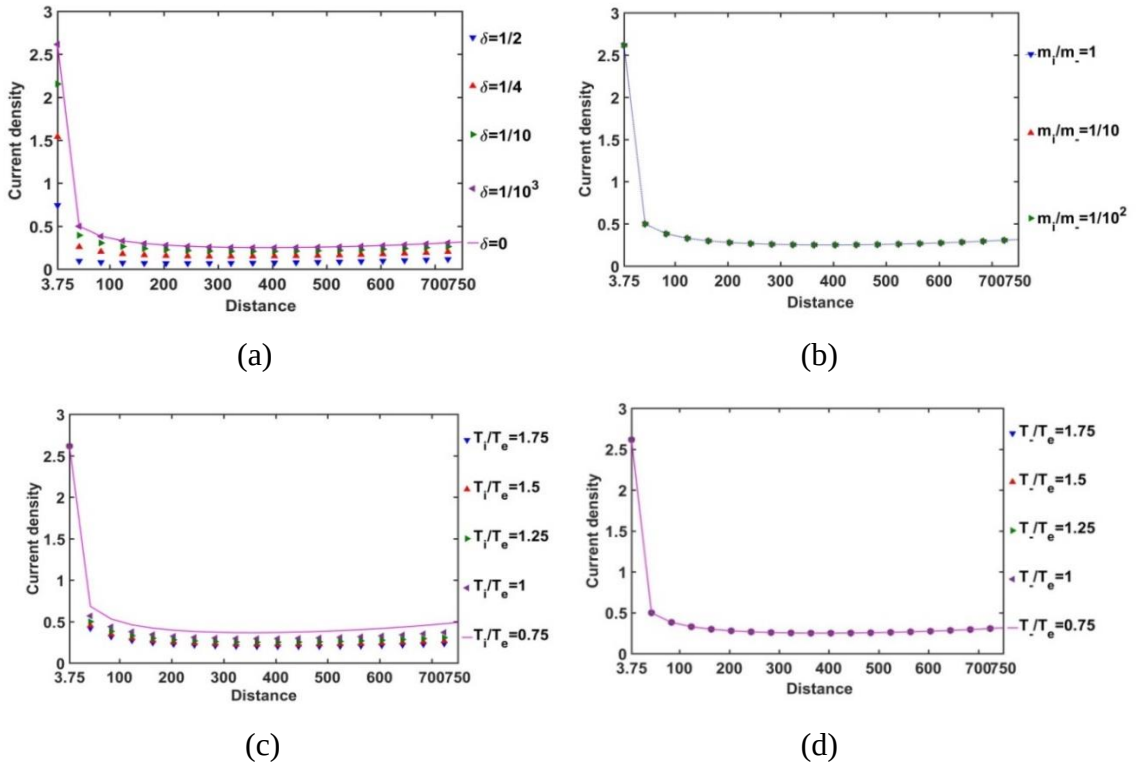

Figure 5.19: *Variation of the SWP electric current density with the Jeans-normalized heliocentric radial distance for different values of the (a) equilibrium negative-to-positive ion density ratio (δ) with fixed $m_i/m_-=1$, $T_i/T_e=1.25$ and $T_-/T_e=1.25$; (b) positive-to-negative ion mass ratio (m_i/m_-) with fixed $\delta=1/1000$, $T_i/T_e=1.25$ and $T_-/T_e=1.25$; (c) positive ion-to-electron temperature ratio (T_i/T_e) with fixed $\delta=1/1000$, $m_i/m_-=1$ and $T_-/T_e=1.25$; and (d) negative ion-to-electron temperature ratio (T_-/T_e) with fixed $\delta=1/1000$, $m_i/m_-=1$ and $T_i/T_e=1.25$.*

As shown in figure 5.19, we speculate the spatial variation of the Bohm-normalized SWP electric current density portrayed for different values of δ, m_i/m_-, T_i/T_e and T_-/T_e. It is seen that the current density decreases with an increase in δ and vice-versa (figure 5.19(a)), like the corresponding SIP case (figure 5.4(a)). The m_i/m_--variation does not affect the net SWP current density (figure 5.19(b)), as in the SIP (figure 5.4(b)). It is seen from figure 5.19(c) that the SWP current density is dependent on the T_i/T_e-value in the same manner, and hence governed by the same physical principles as the SIP current density (figure 5.4(c)). However, the T_-/T_e-variations do not influence the net SWP electric current density, as seen from figure 5.19(d), like the SIP (figure 5.4(d)).

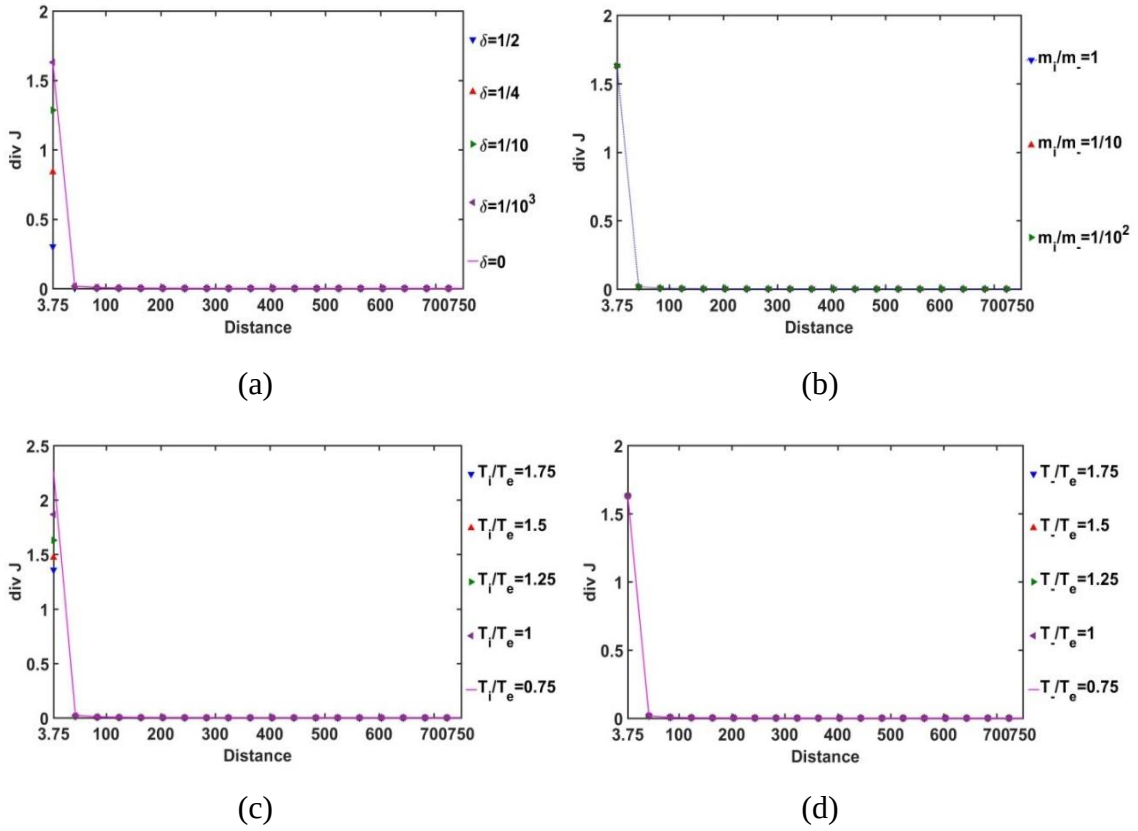

Figure 5.20: *Variation of the divergence of the SWP electric current density (div J) with the Jeans-normalized heliocentric radial distance for different values of the (a) equilibrium negative-to-positive ion density ratio (δ) with fixed $m_i/m_-=1$, $T_i/T_e=1.25$ and $T_-/T_e=1.25$; (b) positive-to-negative ion mass ratio (m_i/m_-) with fixed $\delta=1/1000$, $T_i/T_e=1.25$ and $T_-/T_e=1.25$; (c) positive ion-to-electron temperature ratio (T_i/T_e) with fixed $\delta=1/1000$, $m_i/m_-=1$ and $T_-/T_e=1.25$; and (d) negative ion-to-electron temperature ratio (T_-/T_e) with fixed $\delta=1/1000$, $m_i/m_-=1$ and $T_i/T_e=1.25$. The inner distinctions of these similar profiles obviously lie in the multi-parametric variations of current solar plasma relevance as shown herein.*

In figure 5.20, we depict the radial variation of the divergence of the Bohm-normalized SWP electric current density for different values of δ, m_i/m_-, T_i/T_e and T_-/T_e. It is found that the current density is fairly conserved throughout the entire SWP medium, except in the near-SSB regions. There appears no source or sink, as in the SIP case as well, to affect the net charge production and its directional flow in the SWP, except in the near-SSB regions ($\xi \approx 3.75$-30). The finite non-zero positive divergence of the net electric current density in the near-SSB regions is attributable to the high charge density of these regions, unlike the diffuse far-SSB regions ($\xi > 30$). The conservative

nature of the electric current density is independent of any parametric variations, such as δ (figure 5.20(a)), m_i/m_- (figure 5.20(b)), T_i/T_e (figure 5.20(c)) and T_-/T_e (figure 5.20(d)).

5.3.3 COMPARATIVE VALUATION

As a reliability check-up of the presented GES-model based solar plasma analysis with diverse negative ionic species, various properties numerically followed and obtained here can be compared to the realistic scenarios or conventional approaches as shown below.

Table 5.4: Present model versus other models

S. No.	Item	Prediction by us	Prediction by others
1	Negative ion density (δ)	Broader δ-values (0, 0.001, 0.1, 0.25, 0.5) with the observed one (δ=0.001) included.	Experimentally confirmed for sun-like stars, $\delta \approx 0.001$ [3], where every metal atom contributes one electron to form negative ions.
2	Mach number at SSB	For δ=0.001, $M_{SSB}=1.3\times10^{-8}$; supersonic transition occurs at $r \approx 84\ \lambda_J$ (1.68×10^{10} m). So, our model creates observed corona-like regions for supersonic SW origin as per the SSM.	Solar wind (SW) particles originate from the corona, the outermost part of the solar atmosphere. This region is extended to 10-20 times solar radius from the solar surface, i.e., $r \sim$ (40-75) λ_J [11, 17].
3	Mach number at 1 au	$M_{1\ au} \sim 1.13$ for δ=0.001 and $m_i/m_-=1$, $T_i/T_e=T_-/T_e=1.25$, i.e., solar wind particles travel with speed $\sim 3.39\times10^5$ m s^{-1}, fairly matching observations.	i. Slow SW speed 2.5×10^5–4×10^5 m s^{-1} at 1 au [8, 10]; ii. Fast SW speed 4×10^5–8×10^5 m s^{-1} at 1 au [8, 10].
4	Solar boundary	For δ=0.001, the SSB forms at 3.75 λ_J ($=7.5\times10^8$ m).	Radius of the Sun (photospheric radius) is determined as 6.96×10^8 m [18].

5	Plasma constitutive temperature ratio	In our model, T_i/T_e= 0.75, 1, 1.25, 1.5, 1.75.	Observed values of SW constituent temperature ratios from various missions at 1 au: i. Cluster: $T_i/T_e < 0.1$ to $T_i/T_e > 10$ [9, 19]; ii. Explorer 34: $T_i/T_e \sim 0.2$-0.67 [9, 20]; iii. Imp 6, 7, and 8: $T_i/T_e < 0.2$ to $T_i/T_e > 2$ [9, 21]; iv. ISEE 3: $T_i/T_e \sim 0.12$-10 [9, 22]; v. Vela 3 & 4: $T_i/T_e \sim$ less than 0.1 to 2.5 for slow solar wind and 0.17-5.0 for fast solar wind [9, 23]; vi. Wind: $T_i/T_e \sim 0.62$-3.33 [9, 24].
6	Internal structure	Highly populated dense regions lie in ξ=0-0.5, i.e., heliocenter to 10^8 m in SIP, matching with the SSM value.	In the SSM, the highly dense core lies from centre to 2.09×10^8 m [18].
7	Negative ion population	SIP is not favourable to heavy negative ion formation; lower the negative ion mass, higher is its population density and vice-versa.	Observationally, the H^- ion (lightest) accounts for the major part of the continuous absorption of the solar atmosphere due to high population density; other negative ions (rare) have been identified later with advanced spectrophotometry [5, 6].

5.4 CONCLUSIONS

The presented chapter reports a theoretical exploration revealing various relevant equilibrium solar plasma properties. It is founded comprehensively on the modified plasma-wall interaction mechanism-based GES-model formalism. The model is refined methodically with a proper inclusion of the realistic negative ionic effects. The considered spherical solar plasma volume consists of the Boltzmann-distributed inertialess electrons, which are gravito-electrostatically coupled with the positive-negative ionic inertial fluids, via the analytic Poisson formalism on the relevant astrophysical scales. The basic governing equations for the tri-component plasmas are systematically developed for describing both the SIP- and SWP-scaled dynamics moderated by the self-gravity and long-range external gravity, respectively.

An exact numerical analysis of the equilibrium GES-model governing equations reveals an interesting property of the bounded solar plasma volume showing its shrinking nature with an increase in the constitutive negative ion concentration in the SIP medium. However, this GES-shrinking behaviour is not affected by the mass of the negative ions and effective bi-ionic temperature relative to the electronic one (figure 5.1). Such SIP features can be well explicated by the electrostatic shielding effects happening between the opposite polarity plasma constituents. The spatial variation of the electric potential is found to be insensitive to the negative ion concentration, negative ion mass, and effective bi-ionic temperature relative to the electronic temperature in both the SIP and SWP media (figure 5.2 and figure 5.17). The solar plasma flow dynamics is analysed with the Mach number and current density profiles for various relevant physical parametric variations (figures 5.3-5.5 and figures 5.18-5.20). In the SWP, the sonic transition of the Mach number is distinctly ruled by the positive ion-to-electron temperature ratio. The current density is sensitive to the negative ion density as well as the positive ion-to-electron temperature ratio in both the SIP and the SWP media. The self-structurization of the SIP constituents is explored with their radial density variations along with their spatial density gradient behaviours (figures 5.6-5.12). The deviation of the modified SIP from the idealistic quasi-neutrality is explored with the help of the colour-spectral profiles in a defined colour phase space (figures 5.13-5.16). Thus, it is revealed that the negative ionic species considerably affect the SIP in its volume, electric current and positive ion population. In contrast, the SWP is not so sensibly influenced by the negative ion population distribution. Finally, a comparative study of the current key findings with the previous results reported in the literature is performed systematically.

REFERENCES

[1] Vidotto, A. A. The evolution of the solar wind. *Living Reviews in Solar Physics*, 18:3(1)-3(86), 2021.

[2] Schleich, S., Boro Saikia, S., Ziegler, U., Güdel, M., and Bartel, M., NIR wave: A Wave - turbulence - driven solar wind model constrained by PSP observations. *Astronomy and Astrophysics*, 672: A64(1)-A64(14), 2023.

[3] Millar, T. J., Walsh, C., and Field, T. A. Negative ions in space. *Chemical Reviews*, 117(3):1765–1795, 2017.

[4] Wildt, R. Negative ions of hydrogen and the opacity of stellar atmospheres. *Astrophysical Journal*, 90:611-620, 1939.

[5] Branscomb, L. M. and F. Pagel, B. E. Atomic and molecular negative ions in stellar atmospheres. *Monthly Notices of the Royal Astronomical Society*, 118:258-270, 1958.

[6] Vardya, M. S. Role of negative ions in late-type stars. *Memoirs of the Royal Astronomical Society*, 71:249-269, 1967.

[7] Dwivedi, C. B., Karmakar, P. K., and Tripathy, S. C. A gravito-electrostatic sheath model for surface origin of subsonic solar wind plasma. *Astrophysical Journal*, 663:1340-1353, 2007.

[8] Kallenrode, M. *Space Physics: An Introduction to Plasmas and Particles in the Heliosphere and Magnetospheres*. Springer, Heidelberg, 2004.

[9] Wilson III, L. B., Stevens, M. L., Kasper, J. C., Klein, K. G., Maruca, B. A., Bale, S. D., Bowen, T. A., Pulupa, M. P., and Salem, C. S. The statistical properties of solar wind temperature parameters near 1 au. *Astrophysical Journal Supplement Series*, 236:41(1)-41(15), 2018.

[10] Maruca, B. A., Qudsi, R. A., Alterman, B. L., Walsh, B. M., Korreck, K. E., Verscharen, D., Bandyopadhyay, R., Chhiber, R., Chasapis, A., Parashar, T. N., Matthaeus, W. H., and Goldstein, M. L. The trans-heliospheric survey radial trends in plasma parameters across the heliosphere. *Astronomy and Astrophysics*, 675: A196(1)-A196(12), 2023.

[11] Stix, M. *The Sun: An Introduction*. Springer, Berlin, 1991.

[12] Priest, E. *Magnetohydrodynamics of the Sun*. Cambridge University Press, Cambridge, New York, 2014.

[13] Karmakar, P. K. and Dwivedi, C. B. A numerical characterization of the gravito-electrostatic sheath equilibrium structure in solar plasma. *International Journal of*

Astronomy and Astrophysics, 1(4):210-231, 2011.

[14] Sarma, P. and Karmakar, P. K. Solar plasma characterization in Kappa (κ)-modified polytropic turbomagnetic GES-model perspective. *Monthly Notices of the Royal Astronomical Society*, 519(2):2879-2916, 2023.

[15] Gilat, A. *MATLAB: An Introduction with Applications*. Wiley, NJ, 2011.

[16] Livadiotis, G. *Kappa Distributions: Theory and Applications in Plasmas*. Elsevier, Amsterdam, 2017.

[17] Kasper, J. C., Klein, K. G., Lichko, E., Huang, J., Chen, C. H. K., Badman, S. T., Bonnell, J., Whittlesey, P. L., Livi, R., Larson, D., Pulupa, M., Rahmati, A., Stansby, D., Korreck, K. E., Stevens, M., Case, A. W., Bale, S. D., Maksimovic, M., Moncuquet, M., Goetz, K., Halekas, J. S., Malaspina, D., Raouafi, N. E., Szabo, A., MacDowall, R., Velli, M., Wit, T. D., and Zank, G. P. Parker solar probe enters the magnetically dominated solar corona. *Physical Review Letters*, 127:255101(1)-255101(8), 2021.

[18] Carroll, W. and Ostlie, D. A. *An Introduction to Modern Astrophysics*. Cambridge, UK, 2017.

[19] Sahraoui, F., Huang, S.Y., Belmont, G., Goldstein, M. L., Retino, A., Robert, P., and De Patoul, J. Scaling of the electron dissipation range of solar wind turbulence. *Astrophysical Journal*, 777:15(1)-15(11), 2013.

[20] Burlaga, L. F. and Ogilvie, K. W. Heating of the solar wind. *Astrophysical Journal*, 159:659-670, 1970.

[21] Feldman, W. C., Asbridge, J. R., Bame, S. J., and Gosling, J. T. Long-term solar wind electron variations between 1971 and 1978. *Journal of Geophysical Research*, 84(A12):7371-7377, 1979.

[22] Newbury, J. A., Russell, C. T., Phillips, J. L., and Gary, S. P. Electron temperature in the ambient solar wind: Typical properties and a lower bound at 1 AU. *Journal of Geophysical Research*, 103(A5): 9553-9566, 1998.

[23] Hundhausen, A. J. Composition and dynamics of the solar wind plasma. *Reviews of Geophysics*, 8(4):729-811, 1970.

[24] Vech, D., Klein, K. G., and Kasper, J. C. Nature of stochastic ion heating in the solar wind : testing the dependence on plasma beta and turbulence amplitude. *Astrophysical Journal Letters*, 850: L11(1)-L11(6), 2017.